frontiers in Earth Science

ORIGINAL RESEARCH
published: 15 August 2018
doi: 10.3389/feart.2018.00107

Paroxysmal Explosions, Lava Fountains and Ash Plumes at Etna Volcano: Eruptive Processes and Hazard Implications

Sonia Calvari[1]*, *Flavio Cannavò*[1], *Alessandro Bonaccorso*[1], *Letizia Spampinato*[1] and *Alessandra G. Pellegrino*[1,2]

[1] Istituto Nazionale di Geofisica e Vulcanologia - Osservatorio Etneo (INGV-OE), Sezione di Catania, Catania, Italy,
[2] Dipartimento di Scienze Biologiche Geologiche e Ambientali, Università degli Studi di Catania, Catania, Italy

Lava fountains have a major impact on the local population since they cause ash plumes that spread several kilometers above and hundreds of kilometers away from the crater. Ash fallout is responsible for disrupting airports and traffic on the motorways well beyond the area of the volcano itself, as well as affecting the stability of buildings and causing public health issues. It is thus a primary scientific target to forecast the impact of this activity on local communities on the basis of parameters recorded by the monitoring network. Between 2011 and 2015, 49 paroxysmal explosive episodes occurred at two of Mt Etna's five summit craters: the New South-East Crater (NSEC) and the Voragine (VOR). In this paper, we examine the features of the 40 episodes occurring at the NSEC during 2011–2013, and of the 4 events at VOR in December 2015. We study these paroxysms using geophysical monitoring data, characterize the episodes, and analyse all available data statistically. Our main results are two empirical relationships allowing us to forecast the maximum elevation of the ash plume from the average height of the lava fountain, useful for hazard assessment and risk mitigation. For Etna, and using the examples described in this paper, we can infer that wind speed $<10\,m\,s^{-1}$ generally results in strong to intermediate plumes rising vertically above the crater, whereas wind speed $>10\,m\,s^{-1}$ is normally associated with weak plumes, bent-over along the wind direction and reaching lower elevations.

Keywords: Etna volcano, paroxysmal explosive activity, lava fountains, ash plume, thermal cameras

OPEN ACCESS

Edited by:
Roberto Sulpizio, Università degli Studi di Bari Aldo Moro, Italy

Reviewed by:
Geoff Kilgour, GNS Science, New Zealand
Susanna Jenkins, Earth Observatory of Singapore, Singapore

***Correspondence:**
Sonia Calvari
sonia.calvari@ingv.it

Specialty section:
This article was submitted to Volcanology, a section of the journal Frontiers in Earth Science

Received: *06 April 2018*
Accepted: *13 July 2018*
Published: *15 August 2018*

Citation:
Calvari S, Cannavò F, Bonaccorso A, Spampinato L and Pellegrino AG (2018) Paroxysmal Explosions, Lava Fountains and Ash Plumes at Etna Volcano: Eruptive Processes and Hazard Implications. Front. Earth Sci. 6:107. doi: 10.3389/feart.2018.00107

INTRODUCTION

Lava fountains are a mixture of liquid clots and droplets (the pyroclasts) and magmatic gases (H_2O, CO_2, SO_2, CH_4, N_2O, HCl, HF, and CO, in order of decreasing abundance; Allard et al., 2005). They are generated when large volumes of volatiles rapidly exsolve from the magma during its ascent and decompression along the conduit (Wilson et al., 1995). The mixture of gas and pyroclasts emerges from the vent as a jet (Wilson et al., 1995), expanding vertically into an eruptive column, where three main regions can be identified. The lowest portion is the gas-thrust region, and comprises the lava fountains (Sparks et al., 1997; Bonaccorso and Calvari, 2017). Measured ascent velocities

in this region are normally greater than 15 m s^{-1} (Patrick, 2007; Patrick et al., 2007; Sahetapy-Engel and Harris, 2009), and for Etna vary between 33 and 125 m s^{-1} (Calvari et al., 2011; Carbone et al., 2015; Giuffrida et al., 2018), but values of 170, 227, and 405 m s^{-1} have been measured at Montserrat, Sakurajima, and Stromboli volcanoes, respectively (Clarke et al., 2002; Taddeucci et al., 2012; Tournigand et al., 2017). Above the gas-thrust is the convective region, where atmospheric mixing occurs (Sparks et al., 1997; Bombrun et al., 2018), causing a decrease in ascent velocity and lateral wind transport (Carey and Sparks, 1986). The uppermost portion is the umbrella region, where the volcanic plume reaches the zone of neutral buoyancy and spreads out laterally (Carey and Sparks, 1986; Bonadonna and Phillips, 2003). Within the buoyant umbrella region, plume rise rates are less than 15 m s^{-1} (Patrick, 2007; Patrick et al., 2007). Volcanic plume dynamics depend closely on the interaction with the atmospheric wind field. They are classified as strong or weak depending on whether the characteristic plume rise velocity is greater or much smaller than the cross wind speed, respectively (Carey and Sparks, 1986). Thus, strong plumes vertically rise (**Figure 1A**), while weak plumes tend to bend over in the downwind direction (**Figure 1C**) which then start spreading sub-horizontally around the neutral buoyancy level (Carey and Sparks, 1986; Bonadonna and Phillips, 2003). The plume shape has significant effects on the forecast of the fallout area, which is ideally distributed all around the vent in the case of a strong plume and zero wind, and elongated downwind for a weak plume and strong wind. The stronger the wind, the narrower the resulting fallout region from the plume (Andronico et al., 2009). Interestingly enough, the wind speed has important effects not just on the fine-grained portion of the plume, but even on the bombs and ballistics, being able to transport large ejecta for several kilometers down wind, causing damage to cars, solar panels, and windows (Andronico et al., 2015). It is difficult to univocally forecast plume height because it is related to the conditions and properties of the erupting system, such as magma discharge rate (Carey and Sparks, 1986), exsolved volatiles from magma, magma/water interaction (Schmith et al., 2018), and vent geometry (either elongated fissure or near-circular conduit; Wilson and Head, 1981; Wilson et al., 1995). Given that discharge rate and ultimately erupted volume have been measured from the lava fountain height (Calvari et al., 2011; Carbone et al., 2015; Bonaccorso and Calvari, 2017), there must be a direct connection between lava fountain height and maximum plume elevation, although this last parameter is also affected by wind speed (e.g., Bonadonna et al., 2015).

Paroxysmal explosive basaltic activity, especially when occurring at frequently erupting volcanoes, can have a strong impact on the population, air traffic and public health (Andronico et al., 2008, 2009; Martin et al., 2009; Baxter, 2010; Horwell et al., 2017). During 2011–2015, Mt. Etna volcano produced 49 paroxysmal lava fountain episodes, evolving into volcanic plumes that spread for more than 9 km above sea level (a.s.l.) into the atmosphere, and with ash fallout as far as hundreds of km from the vent (e.g., Dellino and Kyriakopoulos, 2003; Azzopardi et al., 2013; Athanassiadou, 2016). It is thus of paramount importance to monitor this activity and analyse the data with the aim of developing routines or tools that might be useful for hazard assessment and impact prediction (Cannavò et al., 2017).

This paper seeks to analyse the data recorded during Etna's recent lava fountaining episodes in order to find possible relationships between measurable parameters. We have used images from the network of fixed thermal and visual cameras installed on the volcano slopes by the Istituto Nazionale di Geofisica e Vulcanologia-Osservatorio Etneo (INGV-OE), and gathered from these several parameters such as lava fountain height, exit velocity, duration of the episode, erupted volume and plume height. Among these, estimates of tephra fall volume are of paramount importance for hazard assessment and risk mitigation during future explosive events, since they are typically based on eruption intensity (eruption rate) and magnitude (total erupted mass; Walker, 1980).

We present an analysis of 44 of the 49 paroxysmal episodes occurring at Etna between 2011 and 2015; the remaining 5 could not be analyzed due to poor visibility from the ground cameras. We have used thermal and visual images recorded by the monitoring network of fixed cameras installed by INGV-OE (Andò and Pecora, 2006; Coltelli et al., 2017) to gather information about the total erupted mass and eruption rate of each episode. We have statistically analyzed the dimensional parameters extracted from the monitoring cameras, such as height of the lava fountain and ash plume vs. time, duration of each episode, erupted volume of pyroclastics (obtained from the camera images) and of lava flows (taken from available published data), time-averaged discharge rate (TADR, here referred only to the pyroclastic portion of the erupted material; Harris et al., 2007) and maximum exit velocities of both the lava fountain and plume. Following Harris et al. (2007), instantaneous effusion rate (IER) is the discharge rate from a vent averaged over a smaller unit of time when compared to TADR, which we consider as averaged over the whole duration of the explosive event. We carried out a rigorous correlation analysis on the measured parameters and tried to find a link among parameters.

ETNA'S ERUPTIVE ACTIVITY

Before 2010, lava fountain episodes at Mt. Etna (**Figures 1**, **2**) were an exceptional activity, normally preceding major flank eruptions, such as those in 1991-93, 2000-01, and 2002-03 (Calvari et al., 1994, 2001; Andronico et al., 2005; Andronico and Corsaro, 2011). However, between January 2011 and December 2013, a sequence of 44 such events occurred from a pit on the east flank of the South-East Crater (SEC), one of the four summit craters of Etna (**Figure 2b**). This activity built up a new summit cone (the New South-East Crater, NSEC, **Figure 2b**; Behncke et al., 2014; De Beni et al., 2015), but no major flank eruptions have followed this activity yet. Bonaccorso and Calvari (2013) explained this apparent paradox by the balance between intruded and extruded magma, which at Etna volcano has been found steady during the last 3–4 decades (Wadge and Guest, 1981; Harris et al., 2011, 2012). This steady

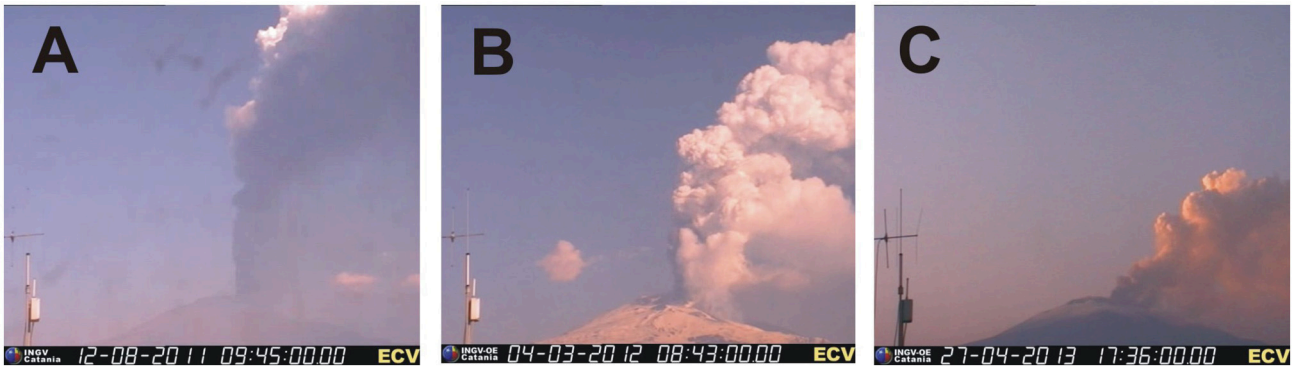

FIGURE 1 | Images taken from the ECV visual camera (see **Table 1** and **Figure 2** for details) showing: **(A)** a strong plume formed during the episode of 12 August 2011 at 09:45; **(B)** an intermediate plume formed during the episode of 4 March 2012 at 08:43; **(C)** a weak plume bending eastward during the episode of 27 April 2013 at 17:36.

output can result either in a few, high-output rate effusive phases, or in several, low-output rate lava fountain events (Bonaccorso and Calvari, 2013). Whatever the cause, it is clear that paroxysmal explosive activity at Etna is becoming increasingly common, thus requiring a greater effort to forecast its possible evolution.

Lava fountains are always associated with ash plumes, often disrupting the air traffic and driveability on the main highway along the east coast of Sicily, where frequent winds blow the ash and cause problems not only to traffic but also public health, agriculture, aviation, and building stability (Andronico et al., 2008; Martin et al., 2009; Baxter, 2010; Horwell et al., 2017). Eruptive columns and ash plumes, associated with the lava fountains, cause a more widespread fallout of ash transported well beyond the boundaries of Sicily and southern Italy and into Greece (Dellino and Kyriakopoulos, 2003) and Malta (Azzopardi et al., 2013).

Lava Fountaining From NSEC, 2011–2013

The 44 lava fountain (LF) episodes at the NSEC between 2011 and 2013 were preceded by deep magma uprising (Del Negro et al., 2013). We distinguished three main phases, separated by two long eruptive pauses (**Table 1**). The first phase lasted from 11 January 2011 to 24 April 2012, and comprised 25 LF events displaying similar features. These are: duration of the Strombolian phase preceding the paroxysmal episode (hours to days); duration of the LF event (hours); maximum height of the LF (800–1,500 m); extension of the lava flow field associated with the explosive event (1–4 km; Behncke et al., 2014); and erupted volume of pyroclastics and lava flows ($\sim 2.5 \times 10^6$ m^3; Calvari et al., 2011; Gouhier et al., 2012; Bonaccorso and Calvari, 2013). The first eruptive pause lasted from April 2012 to February 2013 (**Table 1**). During this pause, only mild and intermittent eruptive activity within the Bocca Nuova summit crater (BN; **Figure 2b**) occurred between July and October 2012, producing a small cinder cone and lava flow field within its crater (Cannata et al., 2015; Slatcher et al., 2015; Spampinato et al., 2015). During the period preceding the second LF phase, ground deformation data from the permanent GPS network revealed an inflation of the volcano due to the pressurization of its plumbing system (e.g., Bruno et al., 2016), whereas gas fluxes showed that no volatile-rich magma was supplied to the shallow (1–2 km below sea level, b.s.l.) volcano feeding system (Spampinato et al., 2015). This suggested that the BN eruptive activity was produced by magma already residing within the shallow plumbing system (Spampinato et al., 2015). A depressurization of the plumbing system was observed when LF activity resumed again in 19 February 2013 (**Table 1**), giving rise to the second eruptive phase that lasted until 27 April 2013, producing 13 additional events (Cannata et al., 2015; Spampinato et al., 2015; Bruno et al., 2016). There was another eruptive pause between April and the end of October 2013, followed by six additional paroxysmal explosive events until the end of that year. This last and third phase was very different from the previous, and comprised the most explosive end-member of the series, occurring on 23 November 2013 (Bonaccorso et al., 2014; Andronico et al., 2015; Carbone et al., 2015; Corradini et al., 2016; Montopoli, 2016). This very short but violent paroxysm produced an exceptionally high LF of over 2.5 km above the crater, and was the only one at the NSEC that did not produce lava flows (Bonaccorso et al., 2014). The third phase also displayed a unique episode (26 October 2013, **Table 1**) during which two craters were erupting together, with the North-East Crater (NEC) producing an ash column that flanked that of the NSEC (Andronico et al., 2018, this volume). As a result of the proximal accumulation of ballistics from the LF around the vent, a new cinder cone (the NSEC) grew on the east flank of the SEC, with a volume of 19×10^6 m^3 (Behncke et al., 2014) by April 2012, and growing up to 50×10^6 m^3 by October 2014 (De Beni et al., 2015). The shallow storage feeding these paroxysmal events, imaged from volcanic tremor and long-period seismic events, is very shallow and located within the volcanic pile between sea level and the ground surface (Cannata et al., 2015) and should represent just the final portion of the uprising path. We know very little about the episode occurring in 2014 (**Table 1**) because of poor weather conditions.

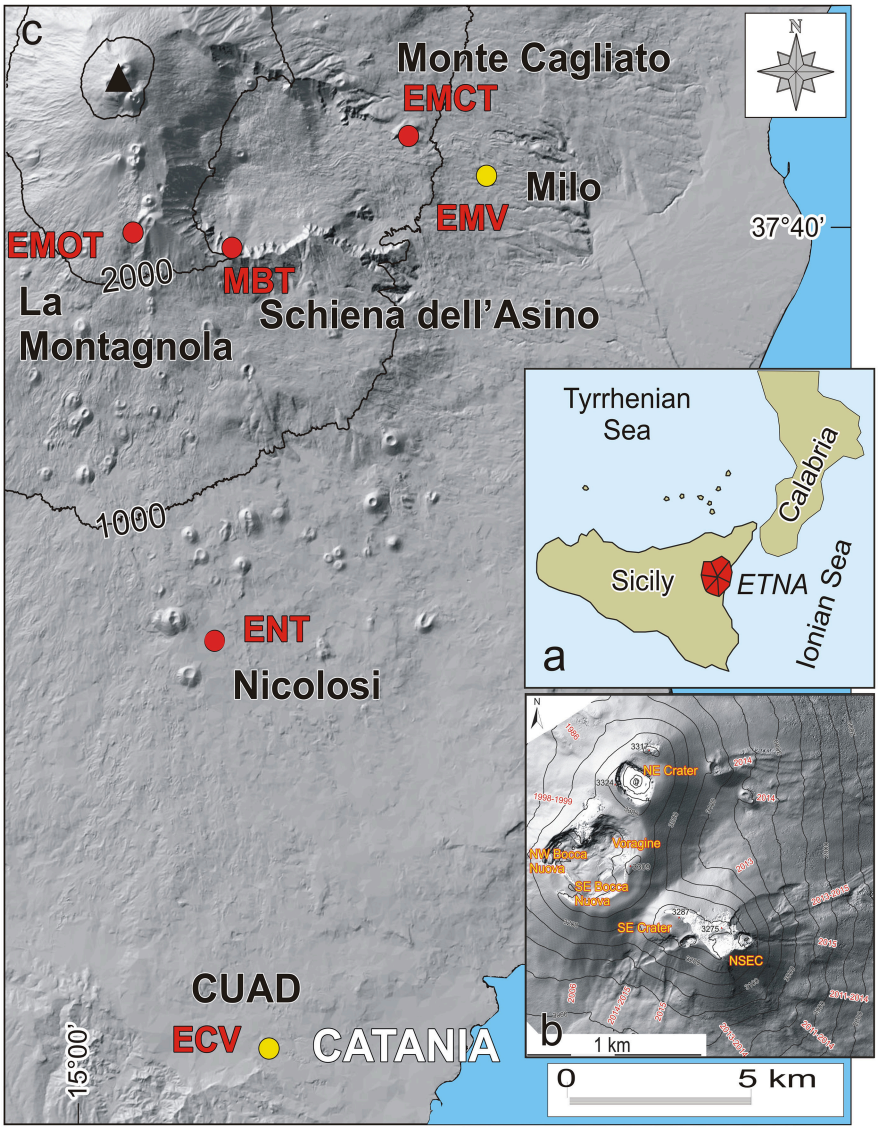

FIGURE 2 | (a) Map of southern Italy, showing the location of Mt. Etna (in red) in the eastern portion of Sicily. **(b)** Map of Etna's summit craters (modified after Neri et al., 2017), with the NE Crater, Voragine, the NW and SE pits of Bocca Nuova, the SE Crater, and the New SE Crater (NSEC) built up on its east flank since 2011. **(c)** Map of the SE flank of Etna volcano, modified after Calvari et al. (2011), showing the location of the thermal (red circles) and visual (yellow circles) monitoring cameras used in this paper. The black triangle shows the position of the summit craters, magnified in **(b)**.

Lava Fountain From VOR, 3–5 December 2015

In January 2015, ash plume emissions started from the Voragine crater (VOR), after 16 years quiescence at this crater (Corsaro et al., 2017; Cannata et al., 2018). Explosive activity from this crater increased in intensity and became almost regular since 27 October, climaxing with a sequence of four paroxysmal events between 3 and 5 December (Vulpiani et al., 2016; Bonaccorso and Calvari, 2017; Neri et al., 2017). The four explosive events interrupted the usual trend of inflation observed at Mt. Etna (Aloisi et al., 2017). They were characterized by decreasing LF maximum heights (from 4.1 to 1.1 km), by lack of associated lava flows, by durations varying between 65 and 114 min, and by a total erupted volume of at least 10×10^6 m^3 dense rock equivalent (Bonaccorso and Calvari, 2017). The eruption columns and ash plume rose vertically with velocities between 150 and 200 m s^{-1}, and the transition from the convective to the umbrella region was observed at ∼8 km height (Vulpiani et al., 2016). In about 10 min the ash plume expanded up to 10–15 km above sea level (a.s.l.; Vulpiani et al., 2016; Corsaro et al., 2017). Tephra fallout accumulated mostly within the summit crater, resulting in a fountain-fed rheomorphic lava of ∼7.2×10^6 m^3 (Corsaro et al., 2017; Neri et al., 2017). The strain data constrained the depth of the magmatic source

TABLE 1 | Eruptive parameters obtained from the analysis of the visual and thermal fixed cameras on each of the paroxysmal episodes.

Event number	Date dd/mm/yy	Vent	Inter time (days)	Duration of Strombolian activity (s)	Start of Lava Fountain (hh:mm)	End of Lava Fountain (hh:mm)	Duration of Lava Fountain (s)	Volume of pyro (m^3)	Volume of pyro Max error (%)	Interp. frames (%)	Cameras	TADR ($m^3\ s^{-1}$)	Hav (m)	Hmax (m)	V_f max ($m\ s^{-1}$)	Duration of lava flow (s)	Lava flow volume (m^3)	Plume type	Max. plume height (m)	V_p max ($m\ s^{-1}$)	Wind speed ($m\ s^{-1}$)
1	12/01/11	NSEC	–	114,000	21:40	23:20	6,000	850,000*	15.4	–	EMOT+ EMV	142	334	830	1.28	21,420	1,685,000§	Strong	9,000*		5.76
2	18/02/11	NSEC	37	15,240	12:34	13:05	1,740	95,250	36.1	–	EMOT	55	95	176	1.81	3,240	700,000§	–			4.81
3	10/04/11	NSEC	51	112,320	09:12	13:22	15,000	1,434,400	11.1	–	EMOT	96	308	1,080“	6.67	18,000	1,038,500§	Strong	7,800**	10.00	7.63
4	12/05/11	NSEC	32	304,320	00:20	03:30	8,220	1,107,380	11.4	4	EMOT	135	331	880	7.62	44,760	1,262,000§	Strong			7.13
5	09/07/11	NSEC	58	42,720	13:45	15:28	6,180	678,370	6.6	–	EMOT	110	520	1,131”	8.19	27,780	1,316,000§	Strong	8,200**	25.00	7.99
6	19/07/11	NSEC	10	16,320	00:00	02:10	7,800	941,360	6.4	–	EMOT	121	487	1,040	8.86	13,140	1,599,500§	Weak			15.05
7	25/07/11	NSEC	6	27,420	01:44	05:50	14,760	1,311,680	14.8	24	EMOT	89	289	823	7.05	19,260	919,000§	Weak			21.68
8	30/07/11	NSEC	5	60,720	19:16	21:20	7,440	777,510	11.0	2	ENT	105	308	1,000	8.75	20,760	2,026,500§	Intermediate			12.33
9	05/08/11	NSEC	6	80,700	21:26	23:20	6,840	975,970	4.8	–	EMOT	143	685	1,097“	6.29	26,640	1,499,000§	Strong			2.78
10	12/08/11	NSEC	7	105,480	08:00	10:18	8,280	815,420	9.7	–	EMOT+ ENT	99	222	900	6.67	20,400	2,303,500§	Strong	9,500§§	6.67	3.39
11	20/08/11	NSEC	8	28,800	06:45	07:50	3,120	342,280	8.6	–	EMOT	110	411	994	4.57	29,400	1,580,500§	Strong	9,300**	16.67	8.69
12	29/08/11	NSEC	9	6,900	03:55	05:05	4,200	476,290	8.1	–	EMOT	113	453	1,080”	9.52	13,800	1,359,500§	Strong	7,800**	10.00	3.66
13	08/09/11	NSEC	10	5,100	06:50	08:18	5,280	553,960	9.5	5	EMOT	105	375	983	7.05	10,800	838,000§	Strong	10,900**	6.67	4.12
14	19/09/11	NSEC	11	55,740	12:40	13:45	3,900	501,500	4.8	88	EMOT	129	509	651	9.05	35,520	430,000§	Weak	5,000**		21.51
15	28/09/11	NSEC	9	61,200	19:05	19:58	3,180	269,570	15.5	37	EMOT	85	271	1,029	13.33	29,340	393,000§	Strong			4.46
16	08/10/11	NSEC	10	14,400	12:58	15:40	10,500	–		–	–	–	–	–		20,760	671,500§	Weak			–
17	23/10/11	NSEC	15	4,380	18:30	20:16	6,360	524,300	14.6	1	ENT	82	238	550	5.00	9,180	950,500§	Intermediate	6,000°°		5.37
18	15/11/11	NSEC	23	10,860	11:15	12:28	4,380	594,480	4.9	–	EMOT	136	590	960	6.29	31,020	1,309,500§	Strong	11,100**		3.41
19	05/01/12	NSEC	51	16,800	05:20	06:55	5,700	818,420	16.0	-	ENT	144	464	1,200	8.33	19,380	1,092,000§	Strong	> 9,000=	13.33	1.05
20	08–09/02/12	NSEC	34	263,280	23:50	05:39	22,080	2,105,970	8.7	–	ENT	95	289	750	2.92	46,500	1,110,000◇	Strong	9,000=		10.37
21	04/03/12	NSEC	25	11,400	06:00	09:31	7,980	1,335,420	11.7	–	ENT	167	444	1,400	14.17	15,240	1,540,000◇	Intermediate	9,000=	13.33	3.22
22	18/03/12	NSEC	14	18,000	07:30	10:03	9,180	1,439,050	22.1	–	ENT	157	669	1,700	11.67	16,620	1,360,000◇	Strong	> 9,000=	6.67	2.79
23	01/04/12	NSEC	14	6,300	01:45	03:38	6,780	901,100	4.8	–	ENT	133	682	1,500	7.50	11,400	1,000,000◇	Strong			15.00
24	12/04/12	NSEC	11	133,320	12:10	15:16	11,160	929,030	6.5	–	ENT	83	649	1,950	10.00	13,380	1,540,000◇	Weak	7,500**	8.33	8.75
25	23–24/04/12	NSEC	11	125,160	23:30	02:20	10,200	641,280	6.4	–	ENT	63	688	1,400	6.67	91,140	1,550,000◇	Intermediate			15.79
26	19/02/13	NSEC	302	6,840	03:48	05:02	4,440	611,340	5.4	–	EMOT	138	634	983“	7.43	3,720	687,500++	Weak			13.31
27	20/02/13–am	NSEC	1	9,000	00:30	01:40	4,200	529,830	6.1	–	EMOT	126	515	1,057	6.29	12,360	687,500++	Intermediate			9.39
28	20/02/13-pm	NSEC	0.5	6,180	12:40	13:46	3,960	295,700	20.9	72	EMOT	75	212	810	5.33	84,600	687,500++	Weak			12.31
29	21/02/13	NSEC	1	13,140	04:00	04:35	2,100	–		–	–	–	–	–		171,000	687,500++	–			–
30	23/02/13	NSEC	2	14,400	18:20	19:16	3,360	426,830	4.2	–	ENT	127	590	1,350	10.00	25,560	687,500++	Weak			24.68
31	28/02/13	NSEC	5	6,180	10:00	10:46	2,760	351,930	6.0	–	EMOT	128	534	937”	6.67	37,080	687,500++	Weak	9,400**		5.26
32	05–06/03/13	NSEC	5	17,760	23:18	00:15	3,420	456,050	6.2	–	MBT	133	615	938“	6.50	156,000	687,500++	Intermediate			8.66
33	16/03/13	NSEC	11	74,580	17:20	18:15	3,300	444,410	8.9	–	EMOT	135	612	926”	4.67	86,400	687,500++	Intermediate			11.66
34	03/04/13	NSEC	18	7,860	11:20	14:45	10,800	1,512,880	6.1	–	ENT	140	485	1,300	5.00	23,400	2,900,000+	Weak	7,800**	1.58	21.78
35	11–12/04/13	NSEC	8	57,600	18:00	12:05	65,100	1,466,621	15.6	–	EMOT	23	189	375	9.90	72,000	700,000+	Intermediate	7,300**	2.22	15.30
36	18/04/13	NSEC	7	124,200	10:30	13:10	8,220	922,730	7.6	39	EMOT+ EMCT	112	494	1,320	3.81	12,000	3,000,000+	Strong	6,900**	11.67	6.51
37	20/04/13	NSEC	2	86,760	15:06	16:35	5,340	480,500	4.6	23	ENT	90	514	1,100	10.00	75,600	1,300,000+	Strong			5.87
38	27/04/13	NSEC	7	518,400	16:36	19:37	10,860	1,038,250	10.7	15	ENT	96	312	900	7.50	25,200	900,000+	Weak	8,500**	10.00	10.89
39	26/10/13	NSEC +NEC	182	46,860	01:45	10:30	32,400	3,628,450	4.5	–	EMOT	83	430	1,100	5.90	28,800	1,600,000+	Strong			1.43

(Continued)

TABLE 1 | Continued

Event number	Date dd/mm/yy	Vent	Inter time (days)	Duration of Strombolian activity (s)	Start of Lava Fountain (hh:mm)	End of Lava Fountain (hh:mm)	Duration of Lava Fountain (s)	Volume of pyro (m^3)	Volume of pyro Max error (%)	Interp. frames (%)	Cameras	TADR (m^3 s^{-1})	Hav (m)	Hmax (m)	V_f max (m s^{-1})	Duration of lava flow (s)	Lava flow volume (m^3)	Plume type	Max. plume height (m)	V_p max (m s^{-1})	Wind speed (m s^{-1})
40	11/11/13	NSEC	16	28,500	02:20	10:30	29,400	–		–	–	–	–	–		61,200	1,700,000+				–
41	16–17/11/13	NSEC	5	158,400	22:41	04:40	21,540	2,409,520	7.9	–	ENT	112	416	1,200	10.00	36,720	500,000+	Strong			1.42
42	23/11/13	NSEC	7	60,000	08:20	10:25	4,620	789,240	3.5	–	ENT	171	1,075	3,400	33.33	30,720	30,000+	Intermediate	12.600‴	13.33	17.19
43	28/11/13	NSEC	5	3,300	20:15	22:39	8,640	944,860	7.4	18	ENT	109	348	700	3.33	21,600	700,000+	Weak			8.11
44	02/12/13	NSEC	4	1,800	19:00	22:20	12,000	–		–	–	–	–	–		21,600	900,000+				–
45	28/12/14	NSEC	391	–	17:16	18:42	5,160	–		–	–	–	–	–		–	2,600,000+				–
46	03/12/15	VOR	340		01:50	03:20	5,400	4,190,000°	1.7	–	ENT	776	1,673	4,100	24.58	No lava flows		Strong	15.000#		2.98
47	04/12/15–am	VOR	1		08:41	10:03	4,920	2,760,000°	2.3	–	ENT	561	1,264	2,600	11.25	No lava flows		Strong	13.400#	11.67	2.69
48	04/12/15-pm	VOR	0.5		20:12	21:17	3,900	1,810,000°	3.3	–	ENT	464	850	2,050	14.17	No lava flows		Strong	13.300#		3.72
49	05/12/15	VOR	1		14:21	16:15	6,840	1,360,000°	3.9	–	EMOT	199	680	1,123	8.57	No lava flows		Strong	13.000#		2.06

Times are in UT format. NSEC, New South-East Crater; NEC, North-East Crater; VOR, Voragine crater. TADR, time averaged effusion rate, calculated only for pyroclastics erupted during the lava fountain over the entire duration of each explosive episode. Cameras labels and locations are in ***Table 2*** *and* ***Figure 2****. Hav, average height of the lava fountain. Hmax, maximum height of the lava fountain. "Saturated value. °Data from Calvari et al. (2011), °Data from Bonaccorso and Calvari (2017), §Data averaged from Ganci et al. (2012) and Behncke et al. (2014), +Data from De Beni et al. (2015), °Data from Behncke et al. (2014), ++Derived from the total volume erupted between 19 February and 16 March 2013 (De Beni et al., 2015) divided by the number (8) of eruptive episodes. **Data from Scollo et al. (2014). §§Data from Scollo et al. (2015). ∞Data from Guerrieri et al., 2015." "Data from Corradini et al. (2016). #Data from Vulpiani et al. (2016). =Data from this work. Gray lines indicate poor weather conditions and lack of visibility from cameras.*

at ∼ 1.5 km b.s.l. (Bonaccorso and Calvari, 2017). This is much deeper than the magmatic source at sea level inferred for the lava fountain episodes at the NSEC (Bonaccorso et al., 2013a,b; Cannata et al., 2015). The fast transfer from the deepest levels of the plumbing system of basic, undegassed magmas has been considered as the crucial triggering factor leading to the development of exceptionally violent volcanic phenomena (Cannata et al., 2018). Also the time scale for completely refilling the VOR system and renewing magma is very fast, being as short as a few tens of hours (Pompilio et al., 2017).

CAMERA RECORDED DATA

We have used the thermal and visual cameras from the INGV-OE monitoring network (**Figure 2c**) to acquire information about the duration of the eruptive activity, such as the start and end of the Strombolian activity preceding the paroxysm, of the lava fountain, of the lava flows, exit velocity, as well as the height of lava fountains. **Table 2** reports the characteristics of the cameras used in this study. Additional information can be found in Andò and Pecora (2006) and Coltelli et al. (2017). Details on the time and kind of eruptive activity for each episode, as well as its duration, are listed in **Table 1**, which also contains the erupted volumes of pyroclastics for each event. These have been obtained, following the approaches of Calvari et al. (2011) and Bonaccorso and Calvari (2017), by integrating the height of the LF obtained from the saturated portion of the thermal images over time at 1 min time lapse, and using the formulas:

$$U = (2gH)^{0.5} \quad (1)$$

$$V = U \times A \times t \quad (2)$$

where U is the mean fluid exit velocity at the vent, H is the LF height, g is the gravity acceleration, V is the fluid volume (gas + pyroclastics) erupted by a LF, A is the vent surface area, and t is the duration of the LF. Vent surface area is calculated considering a circular vent with a diameter of 30 m (Calvari et al., 2011) and supposed constant. Considering a circular shape for the vent area, and multiplying the mean fluid exit velocity at the vent by the vent surface area integrated over time, we transformed the 2D view given by the camera obtaining a 3D volume estimation. The images from the thermal cameras (EMOT, ENT, EMCT, and MBT; **Figure 2c**, **Table 2**) have been used to measure the maximum height of the LF, considered as the saturated portion of each image. Saturation varies with respect to distance between 50°C for the most distant camera (ENT, 15 km; **Figure 2c**) to 100°C for the closest (EMOT, 3 km; **Figure 2c**). The error in the height measurement is ±50 m. We carefully measured the height of the saturated portion, avoiding errors due to clouds interference and to the variable position of the eruptive vent, given that the NSEC, responsible for this eruptive activity, grew by more than 190 m during the lapse of time considered here (Behncke et al., 2014). The heights of the LF at 1 min intervals have then been used to calculate the total fluid erupted volume from Equations (1) and (2), which includes both gas and pyroclastics (Calvari et al., 2011; Bonaccorso and Calvari, 2017). To obtain the volume of pyroclastics from the total volume

TABLE 2 | Characteristics of visual and thermal cameras of the INGV-OE monitoring network used in this paper.

Camera name	Position	Distance from the vent (km)	Vertical FOV (°)	Camera model	Image
EMOT	La Montagnola, 2,600 m a.s.l., south flank	3.0	24	FLIR A40	Thermal
MBT	Schiena dell'Asino, 1,985 m a.s.l., south-east flank	4.9	24	FLIR A40	Thermal
EMCT	Mt. Cagliato, 1,160 m a.s.l., east flank	8.3	25	FLIR A320	Thermal
EMV	Milo, 770 m a.s.l., east flank	10.8	3-47.5	CANON VC-C4R	Visible
ENT	Nicolosi, 730 m a.s.l., south flank	15.0	24	FLIR A40	Thermal
ECV	Catania Nesima, 35 m a.s.l., south flank	26.7	3-47.5	CANON VC-C4R	Visible

*See **Figure 2c** for their location.*

of erupted fluid (gas + pyroclastics), we have considered 0.18% as the ratio between the volumes of magma and fluids within the eruptive column as typical for Etna's fountains (e.g., Donnadieu et al., 2016). This 0.18% between the pyroclastic portion of the LF and the total erupted fluids (gas + pyroclasts), derives from the average volumetric growth of the NSEC cone during the first 12 paroxysmal episodes. In fact, most of the LF fallout accumulates all around the vent, causing the fast growth of the NSEC cinder cone. The NSEC cone volume was measured by Behncke et al. (2014) on 31 August 2011, after 12 LF episodes from the NSEC, at $\sim 9.5 \times 10^6$ m^3 dense rock equivalent (DRE). This volume is ~0.18% of the total volume of fluids (gas + pyroclastics, $\sim 5.4 \times 10^9$ m^3) erupted during the first 12 LF events and obtained from Equations (1) and (2). Considering this a constant, we applied the 0.18% to all pyroclastic volume calculations of the LF episodes from the NSEC reported in **Table 1**. For the four paroxysmal episodes of VOR, this value has been calculated individually for each event, showing a significant variability and a general gradual decline (from 0.22 to 0.09%; Bonaccorso and Calvari, 2017). The maximum error on the pyroclastic volume calculation is reported in **Table 1**, and is calculated from the LF height error (±50 m) and its propagation when using Equations (1) and (2).

The lava flow volumes in **Table 1** are taken from Ganci et al. (2012), Behncke et al. (2014) and De Beni et al. (2015), or are averages of more values when available. TADR is related only to the explosive component of each episode and averaged over the whole duration of the paroxysmal explosive event.

Note that the starting and ending times in **Table 1** (in UT format) have been obtained from careful analysis of the images of the closest cameras (3.0 km from the vent, see **Table 2**), and thus refer to surface expression of the eruptive activity. As such, they could be significantly different from those obtained by geophysical data that refer to changes detected in the source region (e.g., Carbone et al., 2015; Spampinato et al., 2015; Bonaccorso and Calvari, 2017). In addition, given the change from Strombolian to LF activity is generally gradual and characterized by a transitional phase (e.g., Spampinato et al., 2008), we have taken as the starting time of the LF activity the moment when tephra fallout began spreading well outside the crater, in a way to minimize errors in volume calculations. In fact, we have observed that during the transitional phase, the jet of magma is highly collimated, and tephra fallout mainly falls back within the crater, with very little contribution to the volume accumulated on the outer flanks of the cone and beyond.

For four of the 44 eruptive episodes at NSEC between January 2011 and December 2013, we lack data because poor weather conditions hampered camera visibility throughout the entire episode. These are: 8 October 2011, 21 February 2013, 11 November 2013, and 2 December 2013 (**Table 1**). However, in the next section we also considered these episodes when analyzing the relationships between pause interval and total erupted volume. When instead cloud coverage was partial, we have interpolated the missing values. In addition, the 19 September 2011 event (**Table 1**) allowed visibility for only 7 min out of 65, thus in this case most of the erupted volume has been extrapolated on the basis of available data and must be considered a minimum, given that the climax of the LF has been lost. We have analyzed 6333 frames to extract dimensional parameters of the LF. Of these, 352 have been interpolated because of cloud cover, making a 5.6% data interpolated. The amount of interpolated frames for each LF is indicated in **Table 1**. However, it is worth noting that the two events of 18 April 2013 and 20 April 2013 occurred in poor weather conditions, allowing only 1/3 and 2/3 of their duration to be captured by the cameras. These two volumes must be considered as minimums. **Figure 3** displays the first LF episode from NSEC (A) occurring on 12 January 2011 and (B) the first episode from VOR occurred on 3 December 2015, with the outline of the volcano and the two vent positions. Note the very different size of both the LF (in white-red) and eruptive plumes (bluish to pink).

The ECV visual camera (**Figure 2c**, **Table 2**) has been used to extract the growing height of the eruptive plume, following the method proposed by Scollo et al. (2014). They calibrated the ECV images by projecting the plume on a vertical plane passing through the craters and parallel to the wind direction, taken from the daily wind direction forecast, thus obtaining a grid for the plume height estimation with an estimated error on the height of ±0.5 km. The ECV camera has a field of view allowing a maximum height of 9 km a.s.l., thus higher plumes are not visible. Fifteen out of the 44 episodes occurred during daytime and in good weather conditions, also enabling us to analyse the plume height growth together with LF height growth. These data are displayed in **Figure 5**, with the limit of 9 km a.s.l. due to the camera field of view. Note that **Table 1** reports maximum plume heights, thus most of the values greater than 9 km are taken from existing literature.

In summary, we have analyzed the images of 40 eruptive episodes from the NSEC and 4 from VOR in order to obtain:

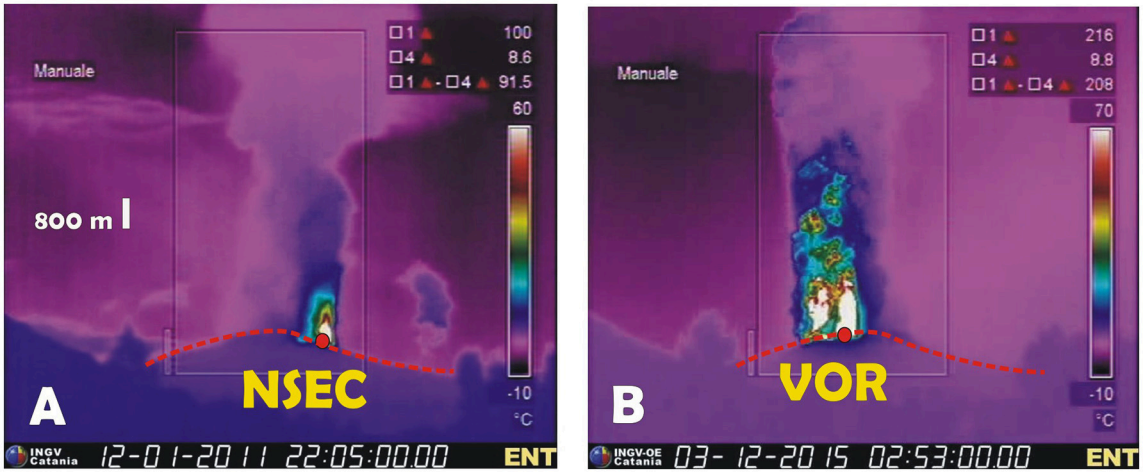

FIGURE 3 | Thermal images from the camera located at Nicolosi, showing **(A)** the first lava fountain episode from NSEC, occurring on 12 January 2011 and taken at 22:05 UT, and **(B)** the first lava fountain episode from VOR on 3 December 2015 and taken at 02:53 UT. The red circles show the position of vent, and the red dotted line is the volcano profile. The white vertical bar in A is for scale. The lava fountain portion is in white-red, the ash plume in bluish-pink. Note the different size of the two episodes, with the VOR lava fountain and plume being much taller and wider.

(1) the duration of the Strombolian activity preceding each episode; (2) the duration of the LF; (3) the total volume of erupted pyroclastics; (4) the time-averaged discharge rate (TADR), referred just to the LF portion of each episode and averaged over the entire duration of the paroxysmal explosive phase; (5) the average and (6) maximum LF heights; (7) the maximum exit velocity of LF; (8) the duration of the lava flow output; (9) the plume type; (10) the maximum elevation of the plume (when lower than 9 km) and the plume growth for 15 events displayed in **Figure 5**; (11) the maximum exit velocity of the plume. Plume type is differentiated into a strong plume when vertical, intermediate when slightly inclined (∼70°) downwind, and weak when markedly bent in a downwind direction (**Figure 1**). These results are listed in **Table 1**. Lava flow volumes and maximum plume heights are taken from available published data as specified in **Table 1**.

STATISTICAL APPROACH

To make the most of the substantial set of paroxysms, we statistically characterized the measured volcanological features with the final aim of analyzing possible correlations among them. Indeed, conducting a correlation analysis that assumes the data follow a normal distribution when, in fact, the data are non-normal, can lead to inaccurate results (e.g., linear correlation analysis is not robust in the presence of non-normality; Kowalski, 1972). To avoid this potential error, we first determined the right distribution of each considered feature. For the analysis, we took into account the following nine features, listed in **Table 1**:

(1) the inter-time between two consecutive paroxysms;
(2) the duration of Strombolian activity before the fountaining event;
(3) the fountain duration;
(4) the duration of the lava flow accompanying the paroxysm;
(5) the mean fountain height;
(6) the maximum fountain height;
(7) the total volume of lava flow associated with the paroxysm;
(8) the total volume of erupted pyroclastics;
(9) the mean wind speed at altitude during the paroxysm.

Each feature was tested for a normal distribution. We used the Shapiro-Wilk (SW) test that is a widely used test of normality in frequency statistics (Shapiro and Wilk, 1965). The null-hypothesis of this test is that the population is normally distributed. The Shapiro-Wilk test is based on the correlation between the data and the corresponding normal scores and performs better than the Kolmogorov-Smirnov (KS) test in recognizing samples from non-normal distributions (Steinskog, 2007). We adopted a confidence level for the test of 5%.

For all the considered features, the test rejected the null-hypothesis of normality, thus we estimated the best distribution among the following ones: *t* location-scale (Rinne, 2011), inverse Gaussian (Chhikara and Folks, 1989), exponential (Balakrishnan and Basu, 1996), logistic and log-logistic (Balakrishnan, 1992). To this set of alternative distributions, we also added the normal distribution to confirm the SW test outcomes. Each distribution was fitted using maximum likelihood estimation. The Akaike information criterion (AIC) was then applied to choose the distribution that better describes the data. The AIC estimates the relative quality of statistical models for a given dataset (Burnham and Anderson, 2003). Given a collection of models for the data, AIC estimates the quality of each model, relative to each of the other models. Thus, AIC provides a means for model selection. The AIC corrected (AICc) for finite sample sizes is defined as:

$$AICc = -2\log\left(L\left(\hat{\theta}\right)\right) + 2k + (2k+1)/(n-k-1) \quad (3)$$

TABLE 3 | Distribution analysis of volcanological features for the set of paroxysms listed in **Table 1**.

Feature	Distribution	I moment (mean)	II moment$^{0.5}$ (standard deviation)
Paroxysm inter-time	Exponential	38 (days)	38 (days)
Duration of Strombolian phase, pre-LF	Inverse Gaussian	53.5 (h)	179.5 (h)
Lava fountain duration	Log-logistic	2.2 (h)	2.1 (h)
Lava flow duration	Log-logistic	9.2 (h)	14 (h)
Mean lava fountain height	Log-logistic	521 (m)	349 (m)
Maximum lava fountain height	t location-scale	1,003 (m)	–
Volume of lava flow	Logistic	1.11×10^6 (m^3)	0.61×10^6 (m^3)
Volume of pyroclastics	Log-logistic	1.06×10^6 (m^3)	1.21×10^6 (m^3)
Wind speed	Log-normal	–	–

L being the model likelihood of the estimated model parameters ($\hat{\theta}$), k the number of parameters, and n the sample size. For all the estimated best distributions, we calculated the first and second moments when existing and finite. Results are reported in **Table 3**, where it is then possible to read the estimated characteristic scales of the features.

We performed a correlation analysis to infer possible hidden relationships among the considered features. Correlation is a bivariate analysis that measures the strengths of association between two variables and the direction of the relationship. In terms of the strength of relationship, the value of the correlation coefficient varies between +1 and −1. When the value of the correlation coefficient lies around ±1, then it is said to be a perfect degree of association between the two variables. As the correlation coefficient value goes toward 0, the relationship between the two variables will be weaker (Hazewinkel, 2001). Commonly, Cohen's standard is used to evaluate the correlation coefficient to determine the strength of the relationship, or the effect size, where correlation coefficients between 0.10 and 0.29 represent a small association, coefficients between 0.30 and 0.49 represent a medium association, and coefficients of 0.50 and above represent a large association or relationship (Cohen, 1988).

There are different types of correlation methodologies. Pearson correlation (parametric test) is the most widely used correlation statistic to measure the degree of the relationship between linearly related variables (Pearson, 1895). For the Pearson correlation, both variables should be normally distributed. Other assumptions include linearity and homoscedasticity. Linearity assumes a straight-line relationship between each of the variables in the analysis and homoscedasticity assumes that data are normally distributed about the regression line (and both variables have a finite variance). These assumptions make the Pearson coefficient unreliable in case of non-normally distributed data. In order to mitigate the distribution effects, we used the Box-Cox transformation (Box and Cox, 1964) to convert the feature distributions into normal ones. In addition, we used the non-parametric tests of Spearman rank (Spearman, 1904) and Kendall rank (Kendall and Gibbons, 1990) correlations to measure the degree of association between two variables without any assumptions about the distribution of the data.

Based on the statistical analysis of the parameters obtained from analyzing the camera images, considering all the three cited coefficients, the correlation analysis confirms that the only significant/large associations are those for the self-explanatory feature pairs:

- volume of pyroclastics and fountain duration (0.66 of mean correlation);
- mean and maximum fountain heights (0.76 of mean correlation).

Nevertheless, it is important to underline that the above statistical analysis is valid for the considered set of volcanological data and should not be generalized outside the considered time interval without further accurate studies.

LAVA FOUNTAIN AVERAGE HEIGHT VS. PLUME MAXIMUM HEIGHT

We investigated the relationship between the average height of the LF (H_F) and the maximum height that reaches the plume (H_P). The average heights of the LF are derived from the thermal images at 1 min intervals. Regarding the measurement of the maximum heights of the plume, in the current literature the work presenting the most complete and detailed catalog is the one published by Scollo et al. (2014), which reports the height measurements of the plume of 19 LF from 10 April 2011 to 27 April 2013. For each event considered, in their **Table 1** the Authors reported three heights respectively estimated from: (1) ECV camera, which, however, cuts the image to 9 km a.s.l.; (2) the MODIS satellite; (3) the SEVIRI satellite. The heights measured with greater precision are those seen by ECV, which records the peak in elevation when below 9 km. Then, with less precision, is the value obtained by MODIS, which has less frequency of satellite passages (and therefore fewer images; 1 every 15 min with 1 km of spatial resolution in the thermal infrared; Corradini et al., 2016). Finally, with even less precision, is the value obtained by SEVIRI, which has a spatial resolution of 3 km and records images every 15 min (Ganci et al., 2012). To obtain a more robust dataset, we therefore used the values obtained from ECV measurements, when H_P was less than 9 km in height, and for other cases ($H_P > 9$ km) we considered the value from MODIS and alternatively, if this was not available, the value of SEVIRI (**Table 4**). For a few cases (**Table 4**) where ECV camera images saturated at 9 km a.s.l., but with the satellite passage providing a lower height because their passage was temporarily distant from the LF climax, we used the ECV camera height. We did not consider the 19 September 2011 and 08 October 2011 episodes due to cloudy weather. Moreover, for the LF of 12 January 2011, we used the plume height reported in Calvari et al. (2011); for the LF of 23 October 2011, we considered the plume height measured by

SEVIRI and reported in Guerrieri et al. (2015); for the LF of 23 November 2013, we considered the height inferred by Corradini et al. (2016) by using a multi-sensor approach considering different satellite instruments such as Meteosat, MODIS and SEVIRI, and finally for the four events of the VOR of 3–5 December 2015, we used the plume heights reported in Vulpiani et al. (2016), obtained by three radar systems (at C and X band) operated by the Italian Department of Civil Protection (**Table 4**).

The relationship between H_F and H_P has some limitations. In fact, it considers a heterogeneous set of data because heights from ECV camera saturate at 9 km a.s.l., and in these cases it is necessary to consider this underestimated value or to resort to the satellites that have a greater resolution error, when often their passage in time is not perfectly synchronous with the maximum height reached by the plume. Despite these limitations, the relationship presents an interesting correlation (**Figure 4**) with a good R^2 of 0.78 for the overall average (Equation 4), and 0.91 for the VOR events only (Equation 5). This provides a useful tool to make a rough forecast of the maximum height reached by the plume once the fountain, well after its initial phase, stabilizes its explosive power and thus its average height, which can be accurately measured in real-time by the cameras monitoring system.

The equations expressing these relationships are:

$$y = 5.26x + 6,830 \quad R^2 = 0.78 \tag{4}$$

$$y = 2.00x + 11,286 \quad R^2 = 0.91 \tag{5}$$

This equals to:

$$Hp = 5.26Hf + 6,830 \ \text{(NSEC)} \tag{6}$$

$$Hp = 2.00Hf + 11,286 \ \text{(VOR)} \tag{7}$$

TIME-DEPENDENT RELATION BETWEEN LAVA FOUNTAIN AND PLUME HEIGHTS

For 15 of the 49 eruptive events, occurring during daytime and with good weather conditions, we also managed to obtain the growing height of the plume over time from the analysis of the images recorded by the ECV camera (**Table 2**). This allows a view of the eruptive plume up to about 9 km a.s.l., estimated using the scheme proposed by Scollo et al. (2014).

The comparison between height of the LF and height of the ash plume is shown in the graphs of **Figure 5**. Although with the limit of the 9 km caused by the camera field of view, from the analysis of **Figure 5** it is possible to observe different behaviors. A first class of events comprises 7 LF (10 April 2011, 20 August 2011, 29 August 2011, 8 September 2011, 18 March 2012, 18 April 2013, and 4 December 2015; **Figure 5**), where the ash plume stays above the 9 km threshold for most of the duration of the LF. These are all strong plumes (**Figure 1A**) formed in wind conditions variable between 2.69 and 8.69 m s^{-1} and with TADR, calculated only for the explosive portion, between 96 and 157 m^3 s^{-1}, and with the outsider event of 4 December 2015 which displayed the exceptional value of 561 m^3 s^{-1} (**Table 1**). A second class of events comprises the two events of 9 July 2011 and 12 August 2011 (**Figure 5**), where the plume remained above 9 km for a short period of time (30 and 52 min, respectively) during

TABLE 4 | Episodes (first column) and dates (second column) of lava fountains of NSEC (events from 1 to 42) and VOR (events from 46 to 49) with the mean height of the fountains (H_F) as obtained from the cam analysis in this study (third column) and maximum height of the plume (H_P) (fourth column) as reported in literature with the sensor utilized (fifth column).

Episode	date (dd/mm/yy)	mean H_F (m)	H_P (m)	H_P reference, sensor utilized
1	12/01/11	334	9,000	Calvari et al. (2011), ECV saturated
3	10/04/11	310	7,800	Scollo et al. (2014), Modis
5	09/07/11	520	9,000	Scollo et al. (2014), ECV saturated
10	12/08/11	636	9,000	Scollo et al. (2014), ECV saturated
11	20/08/11	411	9,300	Scollo et al. (2014), Seviri
12	29/08/11	453	9,000	Scollo et al. (2014), ECV saturated
13	08/09/11	375	9,700	Scollo et al. (2014), Modis
17	23/10/11	238	6,000	Guerrieri et al. (2015), Seviri
18	15/11/11	590	11,100	Scollo et al. (2014), Modis
19	05/01/12	644	9,000	Scollo et al. (2014), ECV saturated
20	09/02/12	290	8,000	Scollo et al. (2014), ECV & Seviri
21	04/03/12	450	9,500	Scollo et al. (2014), Modis
22	18/03/12	640	11,000	Scollo et al. (2014), Modis
24	12/04/12	112	7,500	Scollo et al. (2014), ECV
31	28/02/13	534	9,400	Scollo et al. (2014), Seviri
34	03/04/13	485	7,500	Scollo et al. (2014), ECV
35	12/04/13	204	7,500	Scollo et al. (2014), ECV
36	18/04/13	165	9,000	Scollo et al. (2014), ECV saturated
38	27/04/13	312	8,500	Scollo et al. (2014), ECV
42	23/11/13	1,075	12,600	Corradini et al. (2016), Seviri + Modis
46	03/12/15	1,743	15,000	Vulpiani et al. (2016), terrestrial radar
47	04/12/15	1,264	13,400	Vulpiani et al. (2016), terrestrial radar
48	04/12/15	926	13,200	Vulpiani et al. (2016), terrestrial radar
49	05/12/15	682	12,800	Vulpiani et al. (2016), terrestrial radar

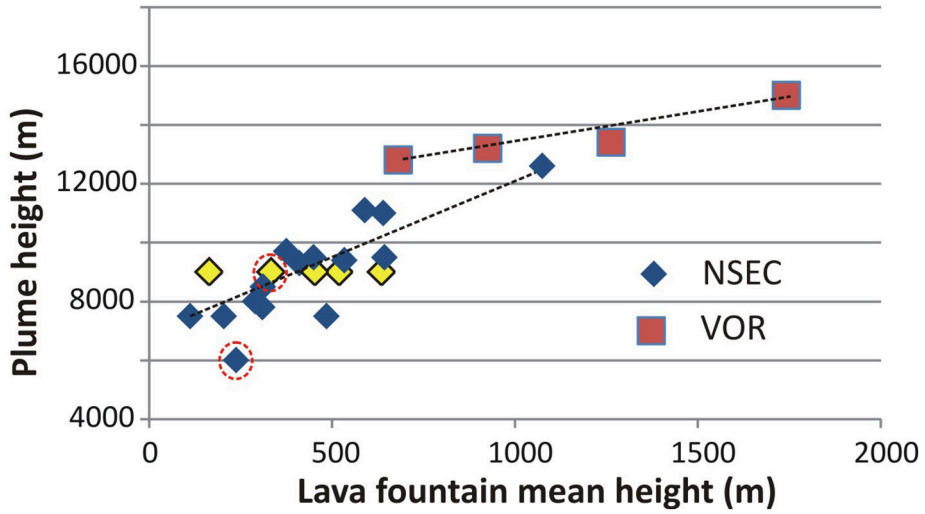

FIGURE 4 | Fountain average height H_F vs. plume height H_P. For the NSEC lava fountains, the H_P values are taken from Scollo et al. (2014) for 19 lava fountains (from 10 April 2011 to 27 April 2013) with the criterion detailed in the text. To this database we added the measurements, highlighted by the red circles, coming from Calvari et al. (2011) for the event of 12 January 2011, and from Guerrieri et al. (2015) for the event of 23 October 2011. The four H_P values of the VOR December 2015 events (red squares) are taken from Vulpiani et al. (2016). The five yellow diamonds show data taken from ECV, with the 9 km a.s.l. limit.

the climax reached by the lava fountains, and decreased soon after and while the LF was still on going. These two events are both strong plumes formed in wind conditions of 3.99 and 7.99 m s^{-1}, and having TADR of 110 and 99 m^3 s^{-1}, respectively, thus comparable to the range of the first class. A different pattern is shown by the 6 events of 4 March 2012, 12 April 2012, 3 April 2013, 12 April 2013, 27 April 2013, and 23 November 2013, where the height of the ash plume increases and decreases together with the height of the LF (**Figure 5**). It is worth noting that the 27 April 2013 plume decline after the end of the LF is not reported in **Figure 5** because it has been observed from thermal images and not from the ECV camera, given that it occurred during the evening and hence with no visibility from this camera. These are intermediate to weak plumes (**Figures 1B,C**) formed in wind conditions comprised between 3.22 and 21.78 m s^{-1} and displaying TADR between 23 and 171 m^3 s^{-1}. Thus, from an overall view of these data, it appears that conditions of strong wind (above ∼10 m s^{-1}) or low TADR (below 100 m^3 s^{-1}), or a combination of these two factors, might favor weak to intermediate plumes that decrease in height soon after or together with the end of the LF. Conversely, conditions of high TADR (above 100 m^3 s^{-1}) and slight wind (below ∼10 m s^{-1}), or a combination of these two factors, involves the formation of strong plumes, with plume heights above 9 km maintained even during the phase of waning LF height (**Figure 5**).

The effect of wind speed on the plume style is clearly visible when comparing the LF events on 12 May 2011 and on 19 July 2011 (**Figure 6**). It is worth noting here that wind speed is sampled every 3 h, thus we lack details of wind variability during an event, and we consider it constant throughout a paroxysmal event. The first event occurred in low wind conditions (7.13 m s^{-1}), with LF maximum height of 880 m, and average of ∼300 m, and with a TADR of 135 m^3 s^{-1} (**Table 1**), allowing the gradual development of a strong plume rising vertically from the vent. As the eruptive phase proceeded, we observed at first, between 00:00 and 01:02, intermittent minor ash emissions (**Figure 6A**) accompanied by a Strombolian to transitional phase, followed between 01:02 and 01:17 by the formation of a weak plume (**Figure 6B**) inclined westward (left) by about 45°; between 01:18 and 01:26 (**Figure 6C**) it passed to an intermediate plume with inclination of ∼70° westward; and from 01:26 to 3:21 giving rise to a strong plume rising vertically from the vent (**Figure 6D**) and spreading laterally (**Figure 6E**); between 3.21 and 3:44 the plume again became transitional (**Figure 6F**) until the end of the eruptive event. An opposite example is given by the event of 19 July 2011, which had a similar TADR (121 m^3 s^{-1}, **Table 1**) and a slightly greater vertical extension of the LF height (1,040 m maximum, 487 m average; **Table 1**), but whose plume formed in conditions of stronger wind (15.05 m s^{-1}). The activity started as pulsating and increasing ash emissions between 00:00 and 00:29 (**Figure 6G**), passing to weak plume (bent about 45° eastward, **Figure 6H**) between 00:29 to 01:38 (with LF about 800 m high), and again at pulsating and decreasing ash emissions between 01:38 and 02:18 (**Figure 6I**), until the end of the event. Thus, **Figure 6** displays the importance of wind speed and IER in determining the plume style, passing from no plume to weak, intermediate and then to strong plume with increasing IER (from 43 to 67, 85 and 130 m^3 s^{-1}, respectively) and in conditions of low wind (7.13 m s^{-1}, **Table 1** and **Figures 6A–E**). Vice-versa, the opposite change occurs when IER vanishes (**Figures 6E,F**, from 119 to 0 m^3 s^{-1}). On the contrary, if wind speed is strong (15.05 m s^{-1} in the case of the 19 July 2011 event, **Table 1** and **Figures 6G–I**), then also a powerful LF ∼800 m high (with IER up to 158 m^3 s^{-1}, **Figure 6H**) is unable to form a strong plume

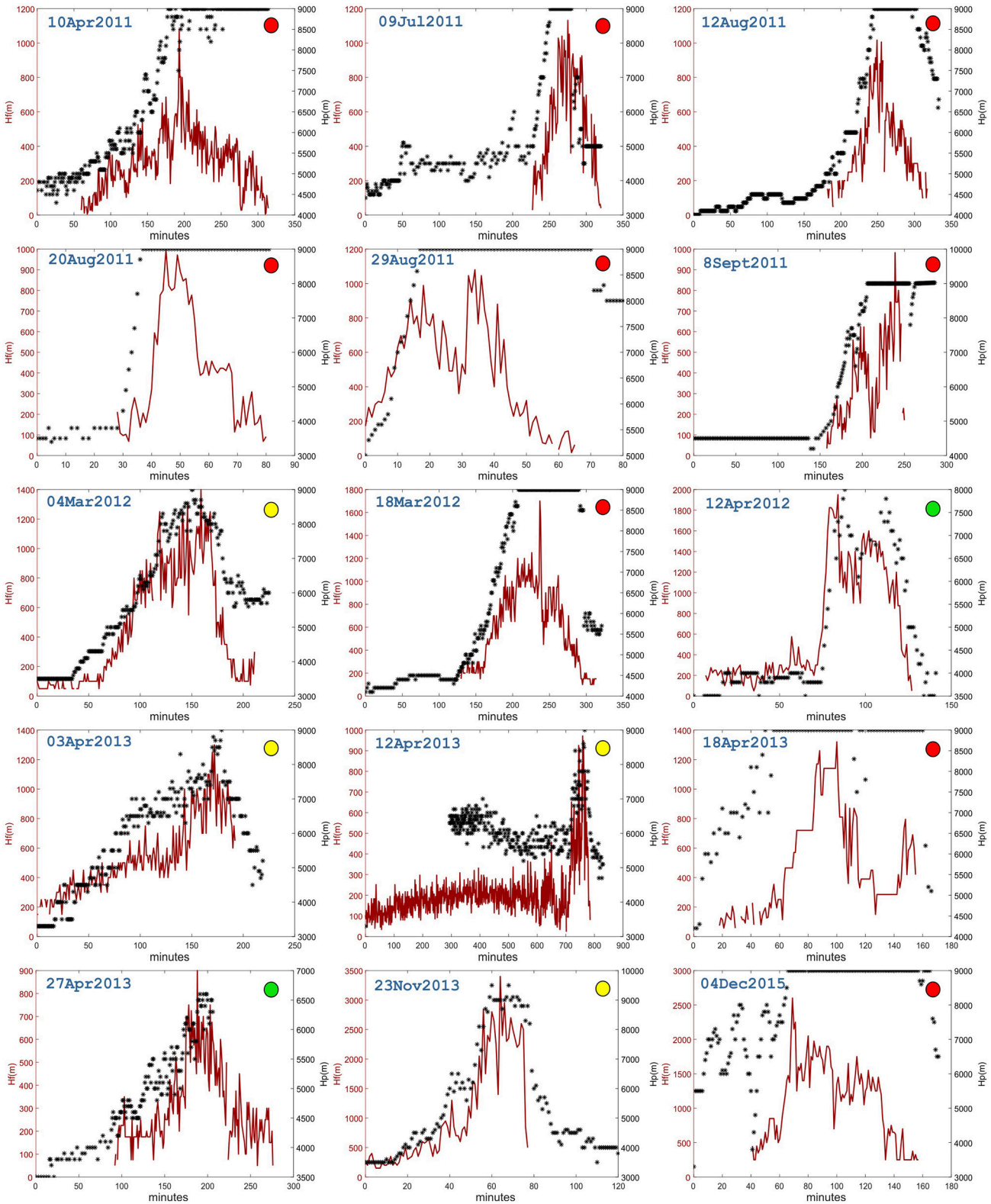

FIGURE 5 | Heights of the ash plume (black stars) measured up to the 9 km a.s.l. limit of the field of view of the ECV camera (see **Table 2** for details) and of the lava fountains (red line) for 15 episodes, with their plume classification (Strong plume with red circle, Intermediate plume with yellow circle and Weak plume with green circle; see also **Figure 1**), occurring during daytime and good weather conditions between 2011 and 2015. Note that the diagrams are not all on the same scale axes. The event of 27 April 2013 misses the final part of plume height (after the peak of the lava fountain) as it occurred at night.

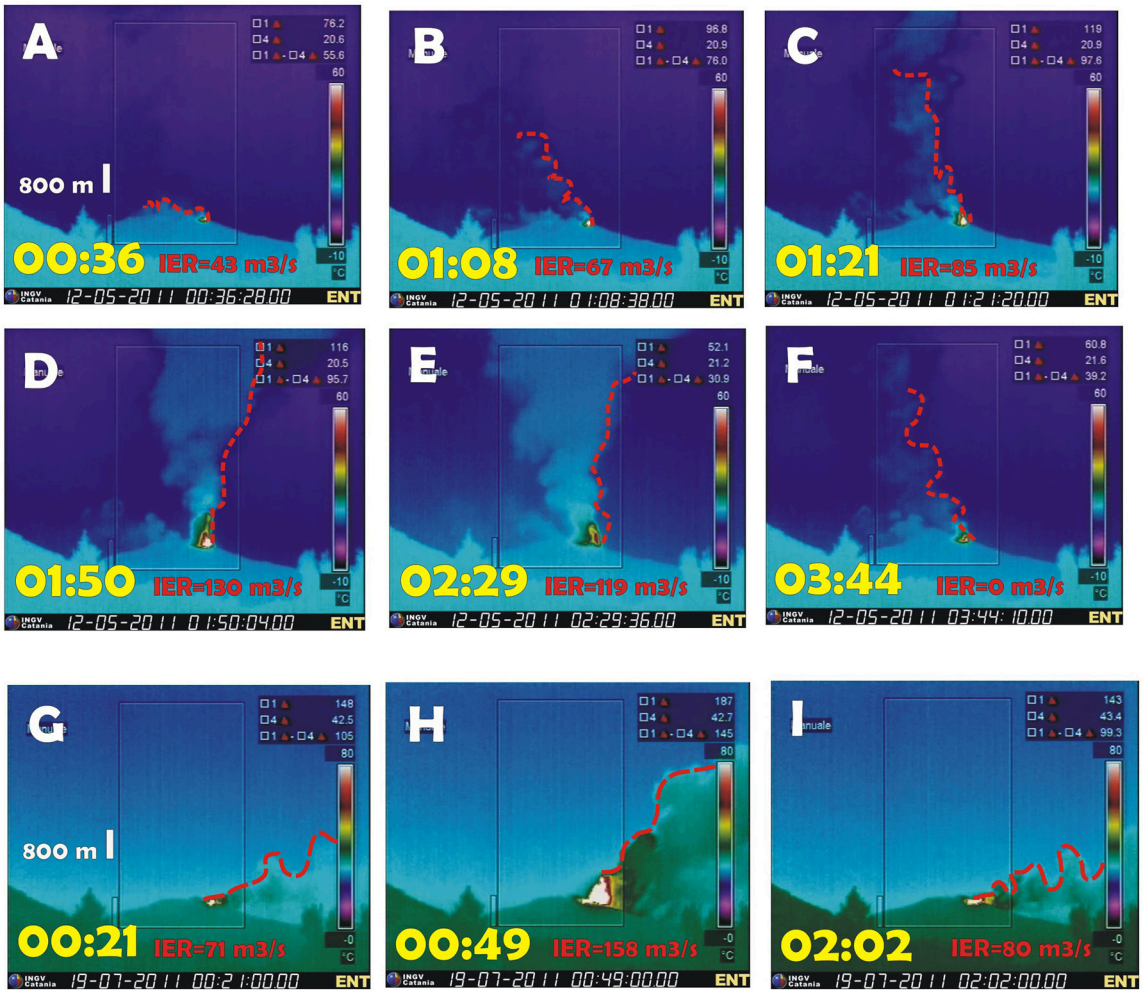

FIGURE 6 | Thermal images recorded by the fixed camera of Nicolosi, south flank of the volcano (ENT, see **Table 2** for details), showing the variability of the plume inclinations (bounded by the red striped line) for the episode of 12 May 2011 **(A–F)**, producing a strong plume **(D,E)**, and for the episode of 19 July 2011 **(G–I)**, giving rise to a weak plume. Eruption parameters are in **Table 1**. In yellow is time (UT), in red Instantaneous Effusion Rate (IER; Harris et al., 2007). The vertical white line in **(A,G)** is for scale. See text for further details.

(**Figures 6G–I**). It is worth noting that the two events reported in **Figure 6** have very similar TADR and durations (averaged over the whole duration of the explosive event, 135 and 121 m^3 s^{-1}, and durations of 8,220 and 7,800 s, respectively; **Table 1**) but wind speed is two-fold during the second case (7.13 vs. 15.05 m s^{-1}; **Table 1**).

DISCUSSION

In this paper, we have analyzed 44 paroxysmal explosive events occurring at Mt. Etna between 2011 and 2015, with the aim of analyzing the eruptive process and finding simple relationships among easily measurable parameters that might be useful for hazard assessment and risk mitigation. Using the images recorded by the network of thermal and visual cameras (**Figure 2c**, **Table 2**), we have characterized each event, extracting the parameters listed in **Table 1**. They are: the vent that produced the event (NSEC, VOR or NEC); duration of the Strombolian phase preceding the LF event; starting and ending time and duration of each LF event; volume of erupted pyroclastics and its maximum error; TADR; maximum and average height of the LF; maximum speed of the LF; the lava flow duration when associated to the explosive event; lava flow volume (taken from available published data, as detailed in **Table 1** caption); plume type (either strong, intermediate or weak, see **Figure 1**); maximum plume heights (from available published data, detailed in **Table 1** caption, or from our measurements using the ECV camera image); maximum velocity of plume growth; and wind speed.

Etna's LFs are significantly different from their Hawaiian counterpart. The main difference is the shape of the vent, which is normally linear (fissure) in Hawaii (e.g., Parcheta et al., 2012), and localized (circular vent or bocca) at Etna (e.g., Calvari et al., 2011). In addition, Hawaiian LFs are normally 200–400 m high

(Head and Wilson, 1987; Wolfe et al., 1988), whereas on Etna we measured LF up to 3–4 km in height during the lapse of time here considered (**Table 1**). It is worth noting that during the explosive activity of Kilauea observed on 17 May 2018, when a summit circular vent was active within the Halemaumau Crater (Patrick et al., 2016), a more than 9 km high ash plume was reported[1] This suggests that, considering all other parameters as steady, a circular vent might promote a greater vertical distribution of the erupted ash when compared to a fissure.

Even more than vent geometry, LF heights depend primarily on the amount of exsolved volatiles (Head and Wilson, 1987), with H_2O being the most abundant (92–96 mol%) and turning to zero as soon as the paroxysm ends (Allard et al., 2005). Etnean magmas are very water-rich basalts, with 3.4 wt% H_2O (Métrich et al., 2004) when compared to their Hawaiian counterpart (0.6–0.8 wt% H_2O; Head and Wilson, 1987), thus confirming that LF height can be used as a reliable indication of exsolved magma gas (water) content (Head and Wilson, 1987).

Using the scheme proposed by Newhall and Self (1982), we have used the erupted volume as the primary parameter for estimating the Volcanic Explosivity Index (VEI) of each event. We have attributed to erupted volumes $<0.5 \times 10^6$ m^3 and/or durations of $<$ 1 h a VEI = 2; VEI = 4 for volumes greater than 2.0×10^6 m^3 and/or durations $>$ 3 h; and VEI = 3 for all events in between these two end-members. Most of the explosive events listed in **Table 1** can be classified as eruptions having VEI 3, based on their durations (1–3 h), erupted volumes (between 0.5 and 2 $\times 10^6$ m^3) and eruptive column height (3–15 km). Only a few (e.g., 18 February 2011) have erupted volumes so small ($\sim 95 \times 10^3$ m^3) to be classified as having VEI = 2 (**Table 5**). **Table 5** lists an estimation of VEI for each of the LF events occurring at Etna between 2011 and 2015.

For the events 16, 29, 40, 44, and 45 (**Tables 1**, **5**) where no volumes are available, VEI has been suggested on the basis of duration. Observing the results displayed in **Table 5**, the first phase of activity, from 11 January 2011 to 24 April 2012, is characterized by 20 VEI 3 plus 4 VEI 2 and 1 VEI 4 events, indicating a steady-state of the volcano as already proposed by Bonaccorso and Calvari (2013) on the basis of just volume estimations. The second phase, from 19 February to 27 April 2013, is very short and comprises 7 VEI 2 and 6 VEI 3 events, suggesting that a new input of gas-rich magma entered the shallow supply system (Bruno et al., 2016) that emptied during the July-October 2012 mainly effusive BN activity (Cannata et al., 2015; Slatcher et al., 2015; Spampinato et al., 2015). The third phase, from 26 October to December 2013, showed a significant change in the supply system, involving more than one crater (26 October 2013 event, **Table 1**) and comprising the most explosive NSEC event (23 November 2013, **Table 1**) during which no lava flows have been erupted. This phase comprises 3 VEI 4 and 3 VEI 3 events, is more powerful and variable, and forecasts the activation of the deeper storage and of the VOR crater that was inactive since 1999 (Corsaro et al., 2017; Cannata et al., 2018). The fourth and final phase here considered (3–5 December 2015, **Table 1**) produced 2 VEI 4 and 2 VEI 3 events (**Table 5**) and high volumes erupted in a short time. Also this phase is followed by a mainly effusive eruption, with the degassed magma being quietly erupted by VOR during 17–25 May 2016 (Edwards et al., 2018). Thus, the estimation of VEI over time gives insights on the state of the volcano and its changes, with a steady-state displayed by constant and low VEI (2–3), and significant changes in the supply system marked by an increase in VEI (3–4).

Each paroxysmal event is characterized by three phases, clearly visible in **Figure 5**: (1) an initial gradual increase of the LF heights; (2) a climax; and (3) a sharply declining phase often accompanied by lava flow output, as already observed by Ganci et al. (2012). These phases, following Head and Wilson (1987), reveal: (1) an initial low gas content release, during the eruption of the gas-poor magma resident in the shallow supply system and left over after the end of the previous explosive event; (2) the output of the gas-rich magma pocket intruded into the system and accumulated at depth to form a foam layer (Allard et al., 2005; Calvari et al., 2011); and (3) the exhaustion of the gas within the magma and the fast passage to either strombolian or effusive conditions.

The two sequences described here, produced by the NSEC (40 events) and by VOR (4 events) displayed very different features. **Figure 3** clearly depicts the different size between the first event occurring at the NSEC in 2011 (**Figure 3A**) and the first event of VOR in 2015 (**Figure 3B**), with greater size of both LF and ash plume for the VOR event. In addition, the events from VOR occurred in a very short time (3 days), had TADR comprised between 199 and 776 m^3 s^{-1} and maximum height of the LF between 1,123 and 4,100 m, and durations of 3,900–6,840 s, and did not produce lava flows (**Table 1**). By contrast, the events produced by the NSEC occurred in 3 years, had much lower TADR (23–171 m^3 s^{-1}) and maximum heights of the LF (176–1,950 m), and greater durations (1,740–65,100 s), were accompanied by lava flow output, with the outsider event of 23 November 2013, which, unlike all other NSEC events, did not erupt lava flows and had LF that reached the huge elevation of 3,400 m above the crater, when all other NSEC events were normally in the range 800–1,200 m (**Table 1**). The two different features are compatible with the different depth of the source region, much deeper for VOR (1.5 km b.s.l.; Bonaccorso and Calvari, 2017) and shallower for NSEC (Bonaccorso et al., 2013a,b; Cannata et al., 2015). The deeper source for VOR also results in a more primitive erupted magma (Corsaro et al., 2017). It is worth noting that VOR erupted just pyroclastics, whereas NSEC had weaker LF generally accompanied by the output of degassed lava flows.

All LF events have displayed an associated ash plume, whose size and shape depends essentially on the interplay between the volume of pyroclastics erupted in the unit of time (IER, here calculated at 1 min intervals; Harris et al., 2007) and the wind speed affecting the summit of the volcano at the time of eruption (Bonadonna and Phillips, 2003). **Table 1** shows that in general at Mt. Etna, low wind speed ($<$10 m s^{-1}) results in strong plumes, whereas high wind speed ($>$10 m s^{-1}) causes

[1]ANSA (2018). http://www.ansa.it/sito/notizie/mondo/2018/05/17/hawaii-allarme-rosso-per-colonna-di-cenere-dal-vulcano_cd92ade5-4066-445e-bbf2-464833d0db52.html; https://www.theguardian.com/us-news/2018/may/17/hawaiis-kilauea-volcano-erupts-releasing-30000ft-plume-of-ash.

TABLE 5 | Event numbers (first column) and dates (second column) of lava fountains of NSEC (events from 1 to 45) and VOR (events from 46 to 49).

Event number	Date dd/mm/yy	Vent	Duration of lava fountain (hh:mm)	Volume of pyro (m^3)	TADR ($m^3\ s^{-1}$)	Hav (m)	Plume height (m)	VEI	Q ($kg\ s^{-1}$)	Hp1 (m a.s.l.) This study	Hp2 (m a.s.l.) Sparks et al. (1997)	Hp3 (m a.s.l.) Woodhouse et al. (2013)
1	12/01/11	NSEC	01:40	850,000*	142	334	9,000*	3	375,417	8,587	6,024	8,180
2	18/02/11	NSEC	00:29	95,250	55	95		2	145,060	7,330	4,709	6,431
3	10/04/11	NSEC	04:10	1,434,400	96	308	7,800**	3	253,411	8,450	5,441	7,406
4	12/05/11	NSEC	02:17	1,107,380	135	331		3	357,001	8,571	5,946	8,077
5	09/07/11	NSEC	01:43	678,370	110	520	8,200**	3	290,888	9,565	5,639	7,669
6	19/07/11	NSEC	02:10	941,360	121	487		3	319,822	9,392	5,779	7,855
7	25/07/11	NSEC	04:06	1,311,680	89	289		3	235,499	8,350	5,339	7,270
8	30/07/11	NSEC	01:04	777,510	105	308		3	276,935	8,450	5,568	7,574
9	05/08/11	NSEC	01:54	975,970	143	685		3	378,117	10,433	6,035	8,195
10	12/08/11	NSEC	02:18	815,420	99	222	9,500§§	3	260,972	7,998	5,483	7,461
11	20/08/11	NSEC	00:52	342,280	110	411	9,300**	2	290,716	8,992	5,638	7,668
12	29/08/11	NSEC	01:10	476,290	113	453	7,800**	2	300,518	9,213	5,687	7,733
13	08/09/11	NSEC	01:28	553,960	105	375	10,900**	3	278,031	8,803	5,573	7,582
14	19/09/11	NSEC	01:05	501,500	129	509	5,000**	3	340,766	9,507	5,875	7,982
15	28/09/11	NSEC	00:58	269,570	85	271		2	224,640	8,255	5,274	7,184
16	08/10/11	NSEC	02:55	–	–	–		3?		–	–	–
17	23/10/11	NSEC	01:46	524,300	82	238	6,000°°	3	218,458	8,082	5,236	7,133
18	15/11/11	NSEC	01:13	594,480	136	590	11,100**	3	359,675	9,933	5,958	8,092
19	05/01/12	NSEC	01:35	818,420	144	464	>9,000=	3	380,492	9,271	6,045	8,208
20	08-09/02/12	NSEC	06:08	2,105,970	95	289	9,000=	4	252,754	8,350	5,437	7,401
21	04/03/12	NSEC	02:13	1,335,420	167	444	9,000=	3	443,468	9,165	6,290	8,533
22	18/03/12	NSEC	02:33	1,439,050	157	669	> 9,000=	3	415,412	10,349	6,184	8,393
23	01/04/12	NSEC	01:53	901,100	133	682		3	352,201	10,417	5,925	8,049
24	12/04/12	NSEC	03:06	929,030	83	649	7,500**	3	220,602	10,244	5,249	7,151
25	23-24/04/12	NSEC	02:50	641,280	63	688		3	166,607	10,449	4,881	6,661
26	19/02/13	NSEC	01:14	611,340	138	634		3	364,879	10,165	5,980	8,122
27	20/02/13-am	NSEC	01:10	529,830	126	515		3	334,299	9,539	5,846	7,944
28	20/02/13-pm	NSEC	01:06	295,700	75	212		2	197,881	7,945	5,103	6,957
29	21/02/13	NSEC	00:35	–	–	–		2?		–	–	–
30	23/02/13	NSEC	00:56	426,830	127	590		2	336,638	9,933	5,856	7,958
31	28/02/13	NSEC	00:46	351,930	128	534	9,400**	2	337,904	9,639	5,862	7,965
32	05-06/03/13	NSEC	00:57	456,050	133	615		2	353,375	10,065	5,930	8,056
33	16/03/13	NSEC	00:55	444,410	135	612		2	356,877	10,049	5,946	8,076
34	03/04/13	NSEC	03:00	1,512,880	140	485	7,800**	3	371,215	9,381	6,007	8,157
35	11-12/04/13	NSEC	18:05	1,466,621	23	189	7,300**	3	59,701	7,824	3,742	5,137
36	18/04/13	NSEC	02:17	922,730	112	494	6,900**	3	297,475	9,428	5,672	7,713
37	20/04/13	NSEC	01:29	480,500	90	514		2	238,452	9,534	5,356	7,293
38	27/04/13	NSEC	03:01	1,038,250	96	312	8,500**	3	253,348	8,471	5,441	7,406
39	26/10/13	NSEC+NEC	09:00	2,672,821	83	430		4	218,610	9,092	5,237	7,135
40	11/11/13	NSEC	08:10	–	–	–		4?		–	–	–
41	16-17/11/13	NSEC	05:59	2,409,520	112	416		4	296,436	9,018	5,667	7,706
42	23/11/13	NSEC	01:17	789,240	171	1,075	12,600"“	3	452,700	12,485	6,323	8,577
43	28/11/13	NSEC	02:24	944,860	109	348		3	289,801	8,660	5,634	7,662
44	02/12/13	NSEC	03:20	–	–	–		3?		–	–	–
45	28/12/14	NSEC	01:26	–	–	–		3?		–	–	–
46	03/12/15	VOR	01:30	4,190,000°	776	1,673	15,000#	4	2,056,204	14,632	9,358	12,579
47	04/12/15-am	VOR	01:22	2,760,000°	561	1,264	13,400#	4	1,486,585	13,814	8,604	11,588
48	04/12/15-pm	VOR	01:05	1,810,000°	464	850	13,300#	3	1,229,872	12,986	8,192	11,045
49	05/12/15	VOR	01:54	1,360,000°	199	680	13,000#	3	526,901	12,646	6,577	8,913

NSEC, New South-East Crater; NEC, North-East Crater; VOR, Voragine crater. Duration of the lava fountains and volume of pyroclastics as in ***Table 1****. TADR, time averaged effusion rate, calculated only for pyroclastics erupted during the lava fountain over the entire duration of each explosive event. Hav, average height of the lava fountain. *Data from Calvari et al. (2011). °Data from Bonaccorso and Calvari (2017). **Data from Scollo et al. (2014). §§Data from Scollo et al. (2015). °°Data from Guerrieri et al. (2015). +Data from this study. ""Data from (Corradini et al., 2016). #Data from Vulpiani et al. (2016). Gray lines indicate poor weather conditions and lack of visibility from cameras. VEI has been calculated from Newhall and Self (1982), see text for details. Q is source mass flux, obtained from TADR and magma density, considered as 2,650 kg m^3. Hp1 is the maximum plume height calculated applying (Equations 6 and 7) proposed in this study. Hp2 has been obtained by the equation from Sparks et al. (1997; $H = 1.67\ TADR^{0.259} \times 1{,}000$), and Hp3 from Woodhouse et al. (2013; $H = 0.318\ Q^{0.253} \times 1{,}000$).*

weak plumes, although some exceptions occur. The importance of wind speed is revealed by the examples displayed in **Figure 6**, showing two events with similar duration, TADR and maximum height of the LF, but very different wind speed. **Figure 6** shows that, during a single event formed in conditions of low wind (<10 m s^{-1}), the passage from weak to intermediate and then to a strong plume occurs at increasing IER (or LF height), and vice-versa (**Figures 6A–F**). By contrast, if a similar event develops in conditions of strong wind (>10 m s^{-1}), then the resulting plume will be weak (**Figures 6G–I**). This is in agreement with the predictive models of Bursik (2001) and Woodhouse et al. (2013), who found that windy conditions require an order of magnitude increase in the source mass flux to obtain equivalent rise heights.

These results stress that evaluating paroxysmal explosive activity just on the basis of the total mass eruption rate (e.g., Corsaro et al., 2017), which is averaged over the whole duration of the event, only gives a general idea of the strength of an event. In addition, this parameter being calculated once that the eruption is finished, cannot be used for hazard purposes. If these data are made available in real time, for example using an automated routine (e.g., Cannavò et al., 2017), it is extremely important to take into account the IER measured on a much shorter lapse of time (Harris et al., 2007), given that it is ideally the instantaneous release of pyroclastics that, in steady wind conditions, defines the passage from weak to strong plume and vice-versa.

The statistical analysis on the parameters obtained from the analysis of the camera images and listed in **Table 1** confirms that the only significant associations are those for the feature pairs:

- volume of pyroclastics and fountain duration (0.66 of mean correlation);
- Mean and maximum fountain heights (0.76 of mean correlation).

The measurement of maximum plume height is a difficult parameter to obtain, because at present ground cameras have limits due to their field of view (9 km a.s.l. for the ECV camera used in this study, **Table 2**), and satellite data depend on the proximity of the satellite overpass with respect to the climax of the explosive phase, whose duration is usually quite short at Etna (**Table 1**). However, even with all these limits, if we select the available data opportunely as we did in **Table 4**, then it is possible to find a good relation between maximum plume height and average LF height, which is even better if we consider only the explosive events of VOR, during which no lava flows were involved.

In fact, using selected published parameters of H_p (**Table 4**), we were able to find two empirical formulas that relate the maximum height of the plume with the average LF height, and these might be used for forecasting a plume extent as soon as the average height of the lava fountain stabilizes. Equation (6) can be used if the eruptive crater is unknown, because for example of poor weather conditions, or if the erupting crater is the NSEC. In cases of paroxysms fed by VOR, instead it is better to use Equation (7), which also gives a lower error in the estimation of plume height.

For the lower correlation between H_p and H_F observed for the NSEC events, we consider that lava flows, spreading mainly within the Valle del Bove depression on the east flank of the volcano, where winds normally also blow the ash plume, might heat the atmosphere and increase the duration of the ash plume at high elevations. Using the regression line of these data (**Figure 4** and Equations 6 and 7) as a general formula applicable during the earlier phases of a future eruption, we can forecast the maximum elevation that an ash plume may attain as soon as the lava fountain has reached its climax, measuring this elevation from the thermal images recorded by the monitoring cameras. In addition, knowing wind speed and direction, we can immediately forecast the sector of the volcano that will be involved by ash fallout and its extension.

Figure 5 shows that plume formation is often as quick as lava fountain formation, although ash fallout on the flanks of the volcano can be observed with 20–30 min delay, as a function of wind speed. However, weak to intermediate plumes tend to decline rapidly as soon as the paroxysm ends, whereas strong plumes tend to keep the elevation of >9 km a.s.l. for most of the duration of the eruptive event, thus increasing the possibility that fine ash transported at high elevations into the atmosphere is dispersed by wind for greater distances.

For Etna, and using the examples described in this paper, we can infer that wind speed <10 m s^{-1} generally results in strong to intermediate plumes, whereas wind speed >10 m s^{-1} is normally associated with weak plumes. A second parameter, important for defining plume formation, is IER, whose effect is shown in **Figure 6**. An increasing IER in low wind conditions will give rise to weak, intermediate and then strong plumes with elevation greater than 9 km, with the opposite trend observed when IER vanishes. In conditions of strong wind instead, the plume remains below 9 km and we usually observe just weak plumes. More data, especially from satellite combined with simultaneous ground measurements, and especially with frequently measured wind speed data, are necessary to improve our ability to forecast the extension and growth of ash plumes associated with lava fountains on Etna and other volcanoes.

Equations (6) and (7) can be used for hazard purposes to calculate the maximum height that the ash plume will attain. They have the great advantage of being applied as soon as the LF mean height has been reached. We will use Equation (6) for events where is the NSEC erupting, and Equation (7) when the crater involved is VOR. Two other possibilities are to use the formula proposed by Sparks et al. (1997):

$$H = 1.67 TADR^{0.259} \quad (8)$$

where H is maximum column height (in km) and TADR is mean discharge rate (m^3 s^{-1}), or a similar equation proposed by Woodhouse et al. (2013):

$$H = 0.318 Q^{0.253} \quad (9)$$

where Q is source mass flux measured in kilograms per second, obtained from TADR and from magma density, considered as 2,650 kg m^3 (**Table 5**). However, Equations (8) and (9) are

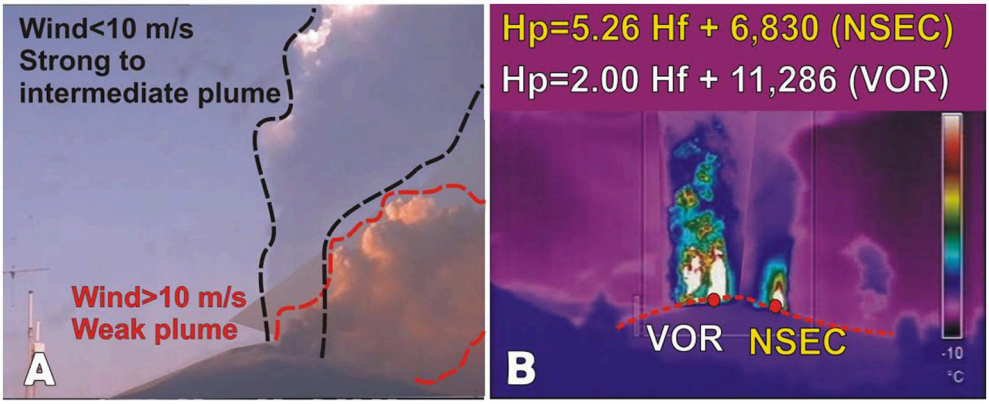

FIGURE 7 | Schemes summarizing the main results obtained in this study. **(A)** At Mt. Etna wind speed greater than 10 m/s produces a weak plume that bends and is elongated along the wind direction (red outline), whereas wind speed below 10 m/s results in strong to intermediate plumes (black outline), causing a lesser impact on the local population (since the ash fallout is mainly concentrated around the crater, although the upper portion of the eruptive column comprising the fine-grained particles is always affected by wind) but a greater effect on aviation (because the elevation of the ash plume is greater). **(B)** We have found two simple relationships between plume (Hp) and lava fountain (Hf) heights that could be used for hazard assessment as soon as the lava fountain average height is reached, expressed by the two equations for VOR (Voragine crater) and for the NSEC (New SE-Crater).

impossible to use for hazard purposes because in order to know the value of TADR or Q, we need to wait until the end of the LF event. **Table 5** presents a comparison between the plume heights from available literature, with those obtained using our Equation (6) for events 1–45 and Equation (7) for the events 46–49 and with values obtained using Equation (8) proposed by Sparks et al. (1997) and Equation (9) proposed by Woodhouse et al. (2013). As reported in **Table 5**, the values from Sparks et al. (1997) mostly result underestimated, whereas those from Woodhouse et al. (2013) are much closer to those obtained from our formulas. However, we must consider that the equation from Sparks et al. (1997) has been obtained using a number of mostly plinian eruptions from several different volcanoes, whereas our equations have been calibrated for Etna. Thus, for hazard purposes, we suggest to interpolate data collected from a single volcano in order to obtain a suitable empirical relationship.

FINAL REMARKS

Etna's LFs are significantly different from their Hawaiian counterpart. The main difference is the shape of the vent, which is normally a fissure in Hawaii, and a circular vent or bocca at Etna. Hawaiian LFs are normally 200–400 m high, whereas on Etna we measured LF up to 3–4 km in height during the lapse of time here considered (**Table 1**). Considering all other parameters as steady, we suggest that a circular vent might promote a greater vertical distribution of the erupted ash when compared to a fissure.

Even more than vent geometry, LF heights depend primarily on the amount of exsolved volatiles, with H_2O being the most abundant (92–96 mol%) and turning to zero as soon as the paroxysm ends. Etnean magmas are very water-rich basalts, with 3.4 wt% H_2O (Métrich et al., 2004) when compared to their Hawaiian counterpart (0.6–0.8 wt% H_2O; Head and Wilson, 1987), thus confirming that LF height can be used as a reliable indication of exsolved magma gas (water) content (Head and Wilson, 1987).

In this paper, we have presented an analysis of the images recorded by Etna's web cameras aimed at quantifying the paroxysmal explosive events occurring between 2011 and 2015. The measured parameters are listed in **Table 1** and their range of variability is reported in **Table 3**. The 44 events here described (**Table 1**) can be divided into two groups: the events from the NSEC normally have VEI 2–3 and lower LF heights, longer event duration, and lower TADR than the events produced by VOR. This is consistent with a deeper source region for the VOR events (e.g., Bonaccorso and Calvari, 2017) allowing deeper, more primitive and gas rich magma to rise rapidly along the conduit (Corsaro et al., 2017; Pompilio et al., 2017), resulting in more hazardous VEI 3–4 eruptions.

An analysis of the measured parameters did not find ready correlations between them, if we exclude those that are directly connected. This is probably due to the many variables affecting the impact of each event, with wind speed and IER playing an important role in defining the maximum extension and style of an ash plume. However, from the data presented, we can observe that in general at Mt. Etna wind speed greater than 10 m s^{-1} produces a weak plume that bends and is elongated along the wind direction, whereas wind speed below 10 m s^{-1} results in strong to intermediate plumes, causing a lower impact on the population (because the ash fallout is mainly concentrated around the crater, although the upper portion of the eruptive column comprising the fine-grained particles is always affected by wind, see **Figure 1A**) but a greater effect on aviation (because the elevation of the ash plume is greater).

For Etna, and using the examples described in this paper, we can infer that wind speed <10 m s^{-1} generally results in strong to intermediate plumes, whereas wind speed > 10 m s^{-1} is normally associated with weak plumes (**Figure 7A**). A second parameter,

important for defining plume formation, is IER (**Figure 6**). An increasing IER in low wind conditions will give rise to weak, intermediate and then strong plumes with elevation greater than 9 km, with the opposite trend observed when IER vanishes. In conditions of strong wind instead, the plume remains below 9 km and we usually observe just weak plumes. We have found a simple relationship between plume and LF heights that could be used for hazard assessment as soon as the LF average height is reached, expressed by the (Equations 6 and 7; **Figure 7B**). The results are better for VOR, because the events produced by this crater did not involve emission of lava flows, thus the whole volume erupted went into the proximal fallout and ash plume. On the contrary, all paroxysms produced by the NSEC, apart from that of 23 November 2013 (Bonaccorso et al., 2014), were associated with lava flow output, thus also involving the emission of degassed magma at the end of each event. In addition, the lava flow spreading mainly within the Valle del Bove, on the east flank of the volcano, where winds normally blow the ash plume, causes heat release and then possibly a plume staying at high elevation for longer time when compared to VOR. More data are necessary to improve our knowledge of these events and our ability to predict their impact, especially by comparing both satellite and ground data and having more frequent wind speed measurements.

AUTHOR CONTRIBUTIONS

All authors listed have made a substantial, direct and intellectual contribution to the work, and approved it for publication.

ACKNOWLEDGMENTS

We thank T. Caltabiano for extracting wind speed and direction from meteorological data provided by the Hydro-Meteorological Service of the Emilia-Romagna Regional Agency for Environmental Protection (ARPA-SIM), and E. Pecora, E. Biale, and M. Prestifilippo for the camera network maintenance. We thank S. Conway for revising the text. A previous version of the manuscript was significantly improved by the comments of two reviewers.

REFERENCES

Allard, P., Burton, M., and Muré, F. (2005). Spectroscopic evidence for a lava fountain driven by previously accumulated magmatic gas. *Nature* 433, 407–410. doi: 10.1038/nature03246

Aloisi, M., Jin, S., Pulvirenti, F., and Scaltrito, A. (2017). The December 2015 Mount Etna eruption: an analysis of inflation/deflation phases and faulting processes. *J. Geodynam.* 107, 34–45. doi: 10.1016/j.jog.2017.03.003

Andò, B., and Pecora, E. (2006). An advanced video-based system for monitoring active volcanoes. *Comput. Geosci.* 32, 85–91. doi: 10.1016/j.cageo.2005.05.004

Andronico, D., Behncke, B., De Beni, E., Cristaldi, A., Scollo, S., Lopez, M., et al. (2018). Magma Budget from Lava and Tephra Volumes erupted during the 25-26 October 2013 Lava Fountain at Mt Etna. *Front. Earth Sci.* 6:116. doi: 10.3389/feart.2018.00116

Andronico, D., Branca, S., Calvari, S., Burton, M. R., Caltabiano, T., Corsaro, R. A., et al. (2005). A multi-disciplinary study of the 2002-03 Etna eruption: insights for into a complex plumbing system. *Bull. Volcanol.* 67, 314–330. doi: 10.1007/s00445-004-0372-8

Andronico, D., and Corsaro, R. A. (2011). Lava fountains during the episodic eruption of South–East Crater (Mt. Etna), 2000: insights into magma-gas dynamics within the shallow volcano plumbing system. *Bull. Volcanol.* 73, 1165–1178. doi: 10.1007/s00445-011-0467-y

Andronico, D., Scollo, S., Caruso, S., and Cristaldi, A. (2008). The 2002–03 Etna explosive activity: tephra dispersal and features of the deposits. *J. Geophys. Res.* 113:B04209. doi: 10.1029/2007JB005126

Andronico, D., Scollo, S., and Cristaldi, A. (2015). Unexpected hazards from tephra fallouts at Mt Etna: the 23 November 2013 lava fountain. *J. Volcanol. Geother. Res.* 304, 118–125. doi: 10.1016/j.jvolgeores.2015.08.007

Andronico, D., Spinetti, C., Cristaldi, A., and Buongiorno, M. F. (2009). Observations of Mt. Etna volcanic ash plumes in 2006: an integrated approach from ground-based and polar satellite NOAA–AVHRR monitoring system. *J. Volcanol. Geother. Res.* 180, 135–147. doi: 10.1016/j.jvolgeores.2008.11.013

Athanassiadou, M. (2016). The Mt Etna SO_2 eruption in December 2015 – the view from space. *R. Meteorol. Soc.* 71, 273–279. doi: 10.1002/wea.2794

Azzopardi, F., Ellul, R., Prestifilippo, M., Scollo, S., and Coltelli, M. (2013). The effect of Etna volcanic ash clouds on the Maltese Islands. *J. Volcanol. Geother. Res.* 260, 13–26. doi: 10.1016/j.jvolgeores.2013.04.019

Balakrishnan, N. (1992). *Handbook of the Logistic Distribution*. New York, NY: Marcel Dekker.

Balakrishnan, N., and Basu, A. P. (1996). *The Exponential Distribution: Theory, Methods, and Applications.* New York, NY: Gordon and Breach.

Baxter P. J. (2010). "Impacts of eruptions on human health," in *Encyclopedia of Volcanoes*, eds H. Sigurdsson, B. Houghton, S. McNutt, H. Rymer, and J. Stix (San Diego, CA: Academic Press), 1035–1043.

Behncke, B., Branca, S., Corsaro, R. A., De Beni, E., Miraglia, L., and Proietti, C. (2014). The 2011–2012 summit activity of Mount Etna: birth, growth and products of the new SE crater. *J. Volcanol. Geother. Res.* 270, 10–21. doi: 10.1016/j.jvolgeores.2013.11.012

Bombrun, M., Jessop, D., Harris, A., and Barra, V. (2018). An algorithm for the detection and characterisation of volcanic plumes using thermal camera imagery. *J. Volcanol. Geother. Res.* 352, 26–37. doi: 10.1016/j.jvolgeores.2018.01.006

Bonaccorso, A., and Calvari, S. (2013). Major effusive eruptions and recent lava fountains: balance between erupted and expected magma volumes at Etna volcano. *Geophys. Res. Lett.* 40, 6069–6073. doi: 10.1002/2013GL058291

Bonaccorso, A., and Calvari, S. (2017). A new approach to investigate an eruptive paroxysmal sequence using camera and strainmeter networks: lessons from the 3–5 December 2015 activity at Etna volcano. *Earth Planet. Sci. Lett.* 475, 231–241. doi: 10.1016/j.epsl.2017.07.020

Bonaccorso, A., Calvari, S., Currenti, G., Del Negro, C., Ganci, G., Linde, A., et al. (2013a). From source to surface: dynamics of Etna's lava foun-tains investigated by continuous strain, magnetic, ground and satellite thermal data. *Bull. Volcanol.* 75:690. doi: 10.1007/500445-013-0690

Bonaccorso, A., Calvari, S., Linde, A., and Sacks, S. (2014). Eruptive processes leading to the most explosive lava fountain at Etna volcano: the 23 November 2013 episode. *Geophys. Res. Lett.* 41, 4912–4919. doi: 10.1002/2014GL060623

Bonaccorso, A., Currenti, G., Linde, A., and Sacks, S. (2013b). New data from borehole strainmeters to infer lava fountain sources (Etna 2011–2012). *Geophys. Res. Lett.* 40, 3579–3584. doi: 10.1002/grl.50692

Bonadonna, C., and Phillips, J. C. (2003). Sedimentation from strong volcanic plumes. *J. Geophys. Res.* 108:2340. doi: 10.1029/2002JB002034

Bonadonna, C., Pistolesi, M., Cioni, R., Degruyter, W., Elissondo, M., and Baumann, V. (2015). Dynamics of wind-affected volcanic plumes: the example of the 2011 Cordón Caulle eruption, Chile. *J. Geophys. Res.* 120, 1–20. doi: 10.1002/2014JB011478

Box, G. E. P., and Cox, D. R. (1964). An analysis of transformations. *J. R. Stat. Soc. Series B* 26, 211–252.

Bruno, V., Ferlito, C., Mattia, M., Monaco, C., Rossi, M., and Scandura, D. (2016). Evidence of a shallow magma intrusion beneath the NE Rift system of Mt. Etna during 2013. *Terra Nova* 28, 356–363. doi: 10.1111/ter.12228

Burnham, K. P., and Anderson, D. R. (2003). *Model Selection and Multimodel Inference: A Practical Information-Theoretic Approach*. New York, NY: Springer Science & Business Media.

Bursik, M. (2001). Effect of wind on the rise height of volcanic plumes. *Geophys. Res. Lett.* 28, 3621–3624. doi: 10.1029/2001GL013393

Calvari, S., Neri, M., Pompilio, M., and Scribano, V. (1994). Etna: eruptive activity. *Acta Vulcanologica* 6, 1–3.

Calvari, S., Salerno, G. G., Spampinato, L., Gouhier, M., La Spina, A., Pecora, E., et al. (2011). An unloading foam model to constrain Etna's 11-13 January 2011 lava fountaining episode. *J. Geophys. Res.* 116:B11207. doi: 10.1029/2011JB008407

Calvari, S., and the whole scientific staff of INGV-Sezione di Catania (2001). Multidisciplinary approach yields insight into Mt. Etna 2001 Eruption. *EOS Trans. Am. Geophys. Union* 82, 653–656. doi: 10.1029/01EO00376

Cannata, A., Di Grazia, G., Giuffrida, M., Gresta, S., Palano, M., Sciotto, M., et al. (2018). Space-time evolution of magma storage and transfer at Mt. Etna Volcano (Italy): the 2015-2016 re-awakening of voragine crater. *Geochem. Geophys. Geosyst.* 19, 471–495. doi: 10.1002/2017GC007296

Cannata, A., Spedalieri, G., Behncke, B., Cannavò F., Di Grazia, G., Gambino, G., et al. (2015). Pressurization and depressurization phases inside the plumbing system of Mount Etna volcano: evidence from a multiparametric approach. *J. Geophys. Res.* 120:1–18. doi: 10.1002/2015JB012227

Cannavò, F. A., Cannata, C., Cassisi, G., Di Grazia, P., Montalto, M., Prestifilippo, E., et al. (2017), A multivariate probabilistic graphical model for real-time volcano monitoring on Mount Etna. *J. Geophys. Res.* 122, 3480–3496. doi: 10.1002/2016JB013512

Carbone, D., Zuccarello, L., Messina, A., Scollo, S., and Rymer, H. (2015). Balancing bulk gas accumulation and gas output before and during lava fountaining episodes at Mt. Etna. *Sci. Rep.* 5:18049. doi: 10.1038/srep18049

Carey, S. N., and Sparks, R. S. J. (1986). Quantitative models of the fallout and dispersal of tephra from volcanic eruption columns. *Bull. Volcanol.* 48, 109–125.

Chhikara, R., and Folks, L. (1989). *The Inverse Gaussian Distribution: Theory, Methodology and Applications.* New York, NY: Marcel Dekker.

Clarke, A. B., Voight, B., Neri, A., and Macedonio, G. (2002). Transient dynamics of vulcanian explosions and column collapse. *Nature* 415, 897–901. doi: 10.1038/415897a

Cohen, J. (1988). *Statistical Power Analysis for the Behavioral Sciences*. New York, NY: Routledge.

Coltelli, M., d'Aranno, P. J. V., de Bonis, R., Guerrero Tello, J. F., Marsella, M., Nardinocchi, C., et al. (2017). The use of surveillance cameras for the rapid mapping of lava flows: an application to Mount Etna Volcano. *Remote Sens.* 9:192. doi: 10.3390/rs9030192

Corradini, S., Montopoli, M., Guerrieri, L., Ricci, M., Scollo, S., Merucci, L., et al. (2016). A multi-sensor approach for volcanic ash cloud retrieval and eruption characterization: the 23 November 2013 Etna Lava Fountain. *Remote Sens.* 8:58. doi: 10.3390/rs8010058

Corsaro, R. A., Andronico, D., Behncke, B., Branca, S., Caltabiano, T., Ciancitto, F., et al. (2017). Monitoring the December 2015 summit eruptions of Mt. Etna (Italy): implications on eruptive dynamics. *J. Volcanol. Geother. Res.* 341, 53–69. doi: 10.1016/j.jvolgeores.2017.04.018

De Beni, E., Behncke, B., Branca, S., Nicolosi, I., Carluccio, R., D'Ajello Caracciolo, F., et al. (2015). The continuing story of Etna's New Southeast Crater (2012–2014): evolution and volume calculations based on field surveys and aerophotogrammetry. *J. Volcanol. Geother. Res.* 303, 175–186. doi: 10.1016/j.jvolgeores.2015.07.021

Del Negro, C., Currenti, G., Solaro, G., Greco, F., Pepe, A., Napoli, R., et al. (2013). Capturing the fingerprint of Etna volcano activity in gravity and satellite radar data. *Sci. Rep.* 3:3089. doi: 10.1038/srep03089

Dellino, P., and Kyriakopoulos, K. (2003). Phreatomagmatic ash from the ongoing eruption of Etna reaching the Greek island of Cefalonia. *J. Volcanol. Geother. Res.* 126, 341–345. doi: 10.1016/S0377-0273(03)00154-9

Donnadieu, F., Freville, P., Hervier, C., Coltelli, M., Scollo, S., Prestifilippo, M., et al. (2016). Near-source Doppler radar monitoring of tephra plumes at Etna. *J. Volcanol. Geother. Res.* 312, 26–39. doi: 10.1016/j.jvolgeores.2016.01.009

Edwards, M. J., Pioli, L., Andronico, D., Scollo, S., Ferrari, F., and Cristaldi, A. (2018). Shallow factors controlling the explosivity of basaltic magmas: the 17–25 May 2016 eruption of Etna volcano (Italy). *J. Volcanol. Geother. Res.* 357, 425–436. doi: 10.1016/j.jvolgeores.2018.05.015

Ganci, G., Harris, A. J. L., Del Negro, C., Guéhenneux, Y., Cappello, A., Labazuy, P., et al. (2012), A year of lava fountaining at Etna: volumes from SEVIRI. *Geophys. Res. Lett.* 39:L06305. doi: 10.1029/2012GL051026

Giuffrida, M., Viccaro, M., and Ottolini, L. (2018). Ultrafast syn-eruptive degassing and ascent trigger high-energy basic eruptions. *Sci. Rep.* 8:147. doi: 10.1038/s41598-017-18580-8

Gouhier, M., Harris, A. J. L., Calvari, S., Labazuy, P., Guéhenneux, Y., Donnadieu, F., et al. (2012). Lava discharge during Etna's January 2011 fire fountain tracked using MSG-SEVIRI. *Bull. Volcanol.* 74, 787–793. doi: 10.1007/s00445-011-0572-y

Guerrieri, L., Merucci, L., Corradini, S., and Pugnaghi, S. (2015). Evolution of the 2011 Mt. Etna ash and SO2 lava fountain episodes using SEVIRI data and VPR retrieval approach. *J. Volcanol. Geother. Res.* 291, 63–71. doi: 10.1016/j.jvolgeores.2014.12.016

Harris, A. J. L., Dehn, J., and Calvari, S. (2007) – Lava effusion rate definition and measurement: a review. *Bull. Volcanol.* 70, 1–22. doi: 10.1007/s00445-007-0120-y

Harris, A. J. L., Steffke, A., Calvari, S., and Spampinato, L. (2011). Thirty years of satellite-derived lava discharge rates at Etna: implications for steady volumetric output. *J. Geophys. Res.* 116:B08204. doi: 10.1029/2011JB008237

Harris, A. J. L., Steffke, A., Calvari, S., and Spampinato, L. (2012). Correction to "Thirty years of satellite-derived lava discharge rates at Etna: implications for steady volumetric output". *J. Geophys. Res.* 117:B08207. doi: 10.1029/2012JB009431

Hazewinkel, M. (2001). *Correlation (in Statistics) in Encyclopedia of Mathematics*. Springer Netherlands.

Head, J. W. III., and Wilson, L. (1987). Lava fountain heights at Pu'u 'O'o, Kilauea, Hawaii: indicators of amount and variations of exsolved magma volatiles. *J. Geophys. Res.* 92:B13. 13,715-13,719.

Horwell, C. J., Sargent, P., Andronico, D., Lo Castro, M. D., Tomatis, M., Hillman, S. E., et al. (2017). The iron-catalysed surface reactivity and health-pertinent physical characteristics of explosive volcanic ash from Mt. Etna, Italy. *J. Appl. Volcanol.* 6:12. doi: 10.1186/s13617-017-0063-8

Kendall, M. G., and Gibbons, J. D. (1990). *Rank Correlation Methods, 5th Edn*. London: Edward Arnold.

Kowalski, C. J. (1972). On the effects of non-normality on the distribution of the sample product-moment correlation coefficient. *Appl. Stat.* 21, 1–12.

Martin, R. S., Watt, S. F. L., Pyle, D. M., Mather, T. A., Matthews, N. E., Georg, R. B., et al. (2009). Environmental effects of ashfall in Argentina from the 2008 Chaitén volcanic eruption. *J. Volcanol. Geother. Res.* 184, 462–472. doi: 10.1016/j.jvolgeores.2009.04.010

Métrich, N., Allard, P., Spilliaert, N., Andronico, D., and Burton, M. (2004). 2001 flank eruption of the alkali- and volatile-rich primitive melt responsible for Mount Etna's evolution in the last three decades. *Earth Planet. Sci. Lett.* 288, 1–17. doi: 10.1016/j.epsl.2004.09.036

Montopoli, M. (2016). Velocity profiles inside volcanic clouds from three-dimensional scanning microwave dual-polarization Doppler radars. *J. Geophys. Res. Atm.* 121, 7881–7900. doi: 10.1002/2015JD023464

Neri, M., De Maio, M., Crepaldi, S., Suozzi, E., Lavy, M., Marchionatti, F., et al. (2017). Topographic maps of Mount Etna summit Crater's Area, 14 December 2015. *J. Maps* 13, 674–683. doi: 10.1080/17445647.2017.1352041

Newhall, C. G., and Self, S. (1982). The volcanic explosivity index (VEI): an estimate of explosive magnitude for historical volcanism. *J. Geophys. Res.* 87, 1231–1238. doi: 10.1029/JC087iC02p01231

Parcheta, C. E., Houghton, B. F., and Swanson, D. A. (2012). Hawaiian fissure fountains 1: decoding deposits—episode 1 of the 1969–1974 Mauna Ulu eruption. *Bull. Volcanol.* 74, 1729–1743. doi: 10.1007/s00445-012-0621-1

Patrick, M. R. (2007). Dynamics of Strombolian ash plumes from thermal video: motion, morphology, and air entrainment. *J. Geophys. Res.* 112:B06202. doi: 10.1029/2006JB004387

Patrick, M. R., Harris, A. J. L., Ripepe, M., Dehn, J., Rothery, D. A., Calvari, S. (2007) – Strombolian explosive styles and source conditions: insights from thermal (FLIR) video. *Bull. Volcanol.* 69:769. doi: 10.1007/s00445-006-0107-0

Patrick, M. R., Swanson, D., and Orr, T. (2016). Automated tracking of lava lake level using thermal images at Kilauea Volcano, Hawai'i. *J. Appl. Volcanol.* 5:6. doi: 10.1186/s13617-016-0047-0

Pearson, K. (1895), Notes on regression and inheritance in the case of two parents. *Proc. R. Soc. Lond.* 58: 240–242.

Pompilio, M., Bertagnini, A., Del Carlo, P., and Di Roberto, A. (2017). Magma dynamics within a basaltic conduit revealed by textural and compositional features of erupted ash: the December 2015 Mt. Etna paroxysms. *Sci. Rep.* 7:4805. doi: 10.1038/s41598-017-05065-x

Rinne, H. (2011). "Location-scale distributions," in *International Encyclopedia of Statistical Science*, ed M. Lovric (Berlin; Heidelberg: Springer), 752–754.

Sahetapy-Engel, S. T., and Harris, A. J. L. (2009). Thermal-image-derived dynamics of vertical ash plumes at Santiaguito volcano, Guatemala. *Bull. Volcanol.* 71, 827–830. doi: 10.1007/s00445-009-0284-8

Schmith, J., Hoskuldsson, A., Holm, P. M., and Larsen, G. (2018). Large explosive basaltic eruptions at Katla volcano, Iceland: fragmentation, grain size and eruption dynamics. *J. Volcanol. Geother. Res.* 354, 140–152. doi: 10.1016/j.jvolgeores.2018.01.024

Scollo, S., Boselli, A., Coltelli, M., Leto, G., Pisani, G., Prestifilippo, M., et al. (2015). Volcanic ash concentration during the 12 August 2011 Etna eruption. *Geophys. Res. Lett.* 42, 2634–2641. doi: 10.1002/2015GL063027

Scollo, S., Prestifilippo, M., Pecora, E., Corradini, S., Merucci, L., Spata, G., et al. (2014). Eruption column height estimation of the 2011-2013 Etna lava fountains. *Ann. Geophys.* 77:S0214. doi: 10.4401/ag-6396

Shapiro, S. S., and Wilk, M. B. (1965). An analysis of variance test for normality (complete samples). *Biometrika* 52, 591–611.

Slatcher, N., James, M. R., Calvari, S., Ganci, G., and Browning, J. (2015). Quantifying effusion rates at active volcanoes through integrated time-lapse laser scanning and photography. *Remote Sens.* 7, 14967–14987. doi: 10.3390/rs71114967

Spampinato, L., Calvari, S., Oppenheimer, C., and Lodato, L. (2008). Shallow magma transport for the 2002-03 Mt. Etna eruption inferred from thermal infrared surveys. J. *Volcanol. Geother. Res.* 177, 301–312. doi: 10.1016/j.jvolgeores.2008.05.013

Spampinato, L., Sciotto, M., Cannata, A., Cannavò, F., La Spina, A., Palano, M., et al. (2015), Multiparametric study of the February–April 2013 paroxysmal phase of Mt. *Etna New South-East crater, Geochem. Geophys. Geosyst.* 16, 1932–1949. doi: 10.1002/2015GC005795.

Sparks, R. S. J., Bursik, M. I., Carey, S. N., Gilbert, J. S., Glaze, L. S., Sigurdsson, H., et al. (1997). *Volcanic Plumes*. Chichester: John Wiley & Sons.

Spearman, C. (1904). The proof and measurement of association between two things. *Am. J. Psychol.* 15, 72–101.

Steinskog, D. J. (2007). A cautionary note on the use of the Kolmogorov-Smirnov test for normality. *Am. Meteor. Soc.* 135, 1151–1157. doi: 10.1175/MWR3326.1

Taddeucci, J., Alatorre- Ibargüengoitia, M. A., Moroni, M., Tornetta, L., Capponi, A., Scarlato, P. et al. (2012). Physical parameterization of Strombolian eruptions via experimentally-validated modeling of high-speed observations. *Geophys. Res. Let.* 39:L16306. doi: 10.1029/2012GL052772

Tournigand, P.-Y., Taddeucci, J., Gaudin, D., Peña Fernández, J. J., Del Bello, E., Scarlato, P., et al. (2017). The initial development of transient volcanic plumes as a function of source conditions. *J. Geophys. Res. Solid Earth* 122, 9784–9803. doi: 10.1002/2017JB014907

Vulpiani, G., Ripepe, M., and Valade, S. (2016). Mass discharge rate retrieval combining weather radar and thermal camera observations. *J. Geophys. Res. Solid Earth* 121, 5679–5695. doi: 10.1002/2016JB013191

Wadge, G., and Guest, J. E. (1981). Steady-state magma discharge at Etna 1971–81. *Nature* 294, 548–550.

Walker, G. P. L. (1980). The Taupo pumice: product of the most powerful known (Ultraplinian) eruption? *J. Volcanol. Geother. Res.* 8, 69–94.

Wilson, L., and Head, J. W. III. (1981). Ascent and eruption of basaltic magma on the Earth and Moon. *J. Geophys. Res.* 86, 2971–3001. doi: 10.1029/JB086iB04p02971

Wilson, L., Parfitt, E. A., and Head, J. W. III. (1995). Explosive volcanic eruptions-VIII. The role of magma recycling in controlling the behaviour of Hawaiian-style lava fountains. *Geophys. J. Int.* 121, 215–225. doi: 10.1111/j.1365-246X.1995.tb03522.x

Wolfe, E. W., Neal, C. A., Banks, N. G., and Duggan, T. J. (1988). Geologic observations and chronology of eruptive events. USGS Prof. *Paper* 1463, 1–98.

Woodhouse, M. J., Hogg, A. J., Phillips, J. C., and Sparks, R. S. J. (2013). Interaction between volcanic plumes and wind during the 2010 Eyjafjallajökull eruption, Iceland. *J. Geophys. Res. Solid Earth* 118, 92–109. doi: 10.1029/2012JB009592

Conflict of Interest Statement: The authors declare that the research was conducted in the absence of any commercial or financial relationships that could be construed as a potential conflict of interest.